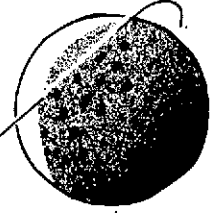


P2

CR-134057



(NASA-CR-134057) EFFECT OF GEOMETRY ON
THE NOSE-REGION FLOW-FIELD OF SHUTTLE
ENTRY-CONFIGURATIONS (Texas Univ.) 43 p
HC \$4.25

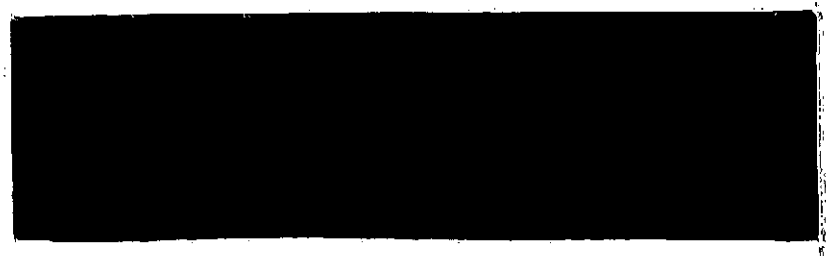
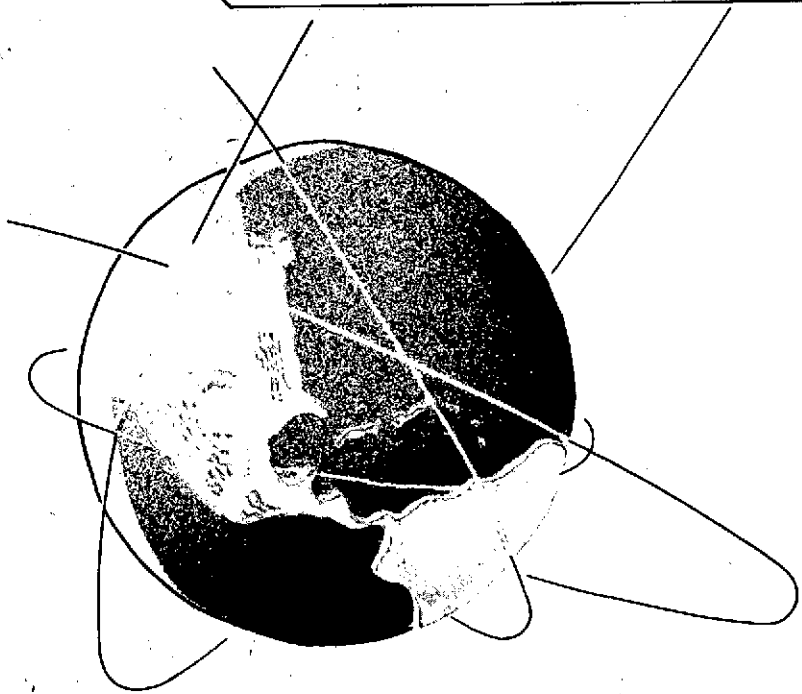
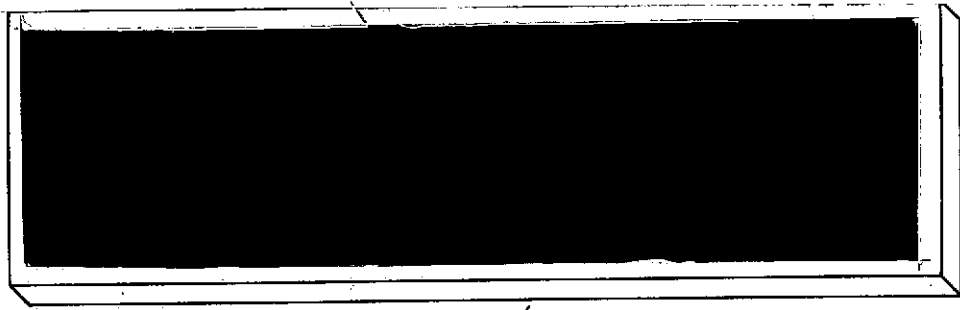
N73-32782

CSCL 22B

Unclas

G3/31

18728



EFFECT OF GEOMETRY ON THE NOSE-REGION
FLOW-FIELD OF SHUTTLE ENTRY-CONFIGURATIONS*

by John J. Bertin and H. Tom Faria

Aerospace Engineering Report 73002

*The authors gratefully acknowledge the support
provided by the Johnson Space Center through
NASA Contract, NAS 9-10976.

Department of Aerospace Engineering and
Engineering Mechanics

The University of Texas at Austin
August 1973



TABLE OF CONTENTS

	Pages
INTRODUCTION	1
EXPERIMENTAL PROGRAM	4
Facility	4
Models	5
Configuration geometry	5
Testing Program	7
DISCUSSION OF RESULTS	8
Surface Oil-Flow Patterns	8
$\alpha = 20^\circ$	9
$\alpha = 25^\circ$	10
$\alpha = 30^\circ$	11
$\alpha = 40^\circ$	12
Schlieren Photographs	13
$\alpha = 20^\circ$	13
$\alpha = 30^\circ$	14
$\alpha = 40^\circ$	15
Surface-Pressure Data	16
CONCLUDING REMARKS	19
REFERENCES	20

INTRODUCTION

In order to determine the convective heat-transfer distribution for the nose region of the space-shuttle entry-configurations, one must describe a three-dimensional flow-field, which may include extensive regions of separated flow. Because of the complexity of the flow-field for the nose region, experimental data are needed to define the relation between the nose geometry and the resultant flow-field.

According to theoretical solutions of the three-dimensional boundary-layer (ref. 1), the boundary layer separates from the leeward generator of a blunted cone at an α equal to the cone half-angle. Separation results from the transverse pressure gradient, i.e., the velocity derivative due to crossflow. The boundary-layer limiting streamlines converge toward the singular point of separation. The separated region is bounded by an ordinary line of separation.

Wang (ref. 2) studied three-dimensional separation-patterns using solutions of the incompressible, laminar boundary-layer near the symmetry plane of an inclined prolate-spheroid. Whereas two-dimensional boundary-layer separation corresponds to the vanishing of skin friction, it is not necessary that the two components of skin friction vanish for three-dimensional separation. The two basic leeward separation concepts used by Wang, i.e., a bubble-type separation and a free-vortex layer are sketched in Fig. 1.

Surface-pressure measurements, oil-flow patterns, and pitot-pressure surveys (ref. 3) indicate a free-vortex-layer type of separation for hypersonic flow past a blunt cone at α s between 6° and 18° . The oil-flow patterns

indicated that the circumferential component of the flow which was initially directed toward the leeward plane of symmetry reversed direction. Two symmetrical separation lines developed downstream of the region where the circumferential component of skin friction passed through zero. At the separation line, the oil accumulated and proceeded to travel down the separation line to the rear of the cone. The fact that the oil near the leeward plane of symmetry continued to flow from the attached region, through the region of zero lateral skin friction, and into the vortex region indicated the longitudinal component of skin friction was always finite. This flow-separation model, contains symmetrical, supersonic, helical vortices close to the surface with an attachment line on the most leeward ray.

Although these separation patterns were obtained for simple shapes, they contain features common to the more complex separated regions of the shuttle entry-configurations. The leeward flow-field of the shuttle is dependent on configuration geometry, on the angle-of-attack, and on the flow conditions. The flow mechanism of greatest importance to the surface environment in the separated region is the free-vortex layer. Reattachment of the vortical flow results in high heating rates to the leeward surface, with local heat-transfer coefficients often exceeding the zero angle-of-attack values. Relatively high leeward-heating has been experimentally observed by Hefner and Whitehead (refs. 4 and 5) for space-shuttle orbiter configurations. Hefner and Whitehead also found that the heat transfer to the lee surface of shuttle-like noses could be reduced by modifying the upper-surface geometry to induce vortex lift-off. The side-view geometry was modified by increasing the initial slope of the lee meridian and then breaking it sharply, which reduced the heating level significantly along 50% of the leeward meridian.

The present paper analyzes experimental data obtained in the University of Texas Supersonic Wind Tunnel (UT SWT) for two orbiter nose geometries. The UT SWT program complemented an experimental program conducted in Tunnel B of Arnold Engineering and Development Center of AEDC (ref. 6). Due to the limited size of the UT SWT test facility, the models represented only the nose section. The model scale was 0.0047. Test data included surface oil-flow pattern photographs, schlieren photographs, and surface pressure measurements. The nominal free-stream Mach number was 4.97 and the free-stream Reynolds number based on an effective body length, ranged from 8×10^6 to 13×10^6 . The effective body length is the length of the model if the entire configuration were present. The effective model length was approximately 15.3 cm (6.0 in.). Thus, a little over 50 percent of the orbiter fuselage was represented.

EXPERIMENTAL PROGRAM

Facility

The tests were conducted in the University of Texas Supersonic Wind Tunnel (UT SWT). The facility is a two-dimensional, blow-down type wind tunnel, using air as the test gas. The test section cross-section dimensions are width 15.3 cm (6.0 in.) by height 17.8 cm (7.0 in.). The test section diverges slightly along its length to accommodate boundary layer growth.

At a free-stream Mach number of 4.97, the free-stream Reynolds number per cm. ranges from 0.49×10^6 to 0.85×10^6 (15×10^6 to 26×10^6 per foot). The usable test-time for the high Reynolds number is approximately 40 seconds in duration.

Two photographs of a typical test setup are presented in Figure 2. The photographs were taken during a series of oil flow tests and, therefore, only one window was in place. When schlieren photographs are taken a similar window is placed on the opposite side of the tunnel. The models were mounted on an "L" shaped floor-mounted sting whose upstream end can be seen at the left in Figure 2. The model base was approximately 7.6 cm (3 in.) upstream of the sting upright. Instrumentation leads were taken out of the tunnel aft of the sting upright to a mercury-filled manometer board from which the surface pressure measurements were obtained. Once the mercury levels reached steady state during the run, the pressure leads were sealed (with a knife switch) and the pressures read. The maximum visual error in reading the manometer boards corresponds to a pressure error of $\pm 7 \times 10^1 \text{ N/m}^2$ (0.01 psi).

Models

The model design philosophy was to generate nose configurations whose surface geometry could be described by analytic functions. The top view planforms were to include both relatively blunt and relatively slender geometries. The cross-section geometries were to provide different cross-flow pressure gradients on the windward surface and different separation patterns on the leeward surface. Only two configurations were built (The University models represented only the nose region of the AEDC models). To satisfy the design philosophy objectives with two models, it was necessary to incorporate an acceptable "extreme" for each of the geometric parameters in one model or in the other.

Configuration geometry. The side-view profiles were the same for the two models (except for a slight difference in the canopy), so as not to introduce yet another geometric variable. The z-dimension of the fuselage was a maximum in the horizontal plane containing the apex of the nose. This ($y = 0$) plane intersected the cross-section at $x = 0.4L$ such that the distance to the keel was one-fourth of the total vertical dimension at this station.

With the exception of the canopy surface and the surface fairings of the wing-root region, the nose geometries can be described by "analytical functions". The analytic functions which define the contours for the two, "clean" configurations are discussed in ref. 7. The actual configurations, which are discussed below, are illustrated in Figs. 3 and 4.

(a) UTN2.- The relatively blunt planform, the relatively flat windward

surface (to reduce the cross-flow pressure gradients), and a leeward geometry which was intended to fix boundary-layer separation were incorporated into the UTN2 configuration as shown in Fig. 3. The apex of the planform in the $y = 0$ plane is a 5:2 ellipse. The windward surface was generated by a parallel translation of the ellipse tangent to the leading edge of the keel. Thus, taking a section in the xz -plane, the trace of the windward surface is a 5:2 ellipse (possibly modified at the downstream end by the wing-root fairing). Because of the relatively blunt character of the windward nose, the wing-root fairing requires only a slight contour modification. In the absence of the canopy, the cross sections of the leeward surface, i.e., y negative, consist of a circular arc, a linear element, and a very flat ellipse. The elements are tangent to each other to avoid sharp corners upstream of $x = 0.25L$. The inclination angle between the linear element and the y -axis is a linear function of x , varying from 25° at $x = 0.02L$ to 15° at $x = 0.16L$ and subsequently varying with x so that the inclination angle is 0° at $x = 0.38L$. The canopy geometry is indicated in the cross-sections of Fig. 3.

(b) UTN7. - As shown in Fig. 4, the UTN7 configuration has the more slender planform and elliptic cross-sections. The apex of the planform in the $y = 0$ plane is 4:1 ellipse. The basic cross-sections (i.e., the cross-sections without the canopy and the wing-root fairing) are composed of two semi-ellipses. The semi-axis ratios for both the windward ellipse and the leeward ellipse are uniquely defined by the maximum y - and z - coordinates for the section at a given station. The canopy geometry and the wing-root fairing modify these elliptic cross-sections, as can be seen in Fig. 4. Because both nose configurations were designed to fair into a common

fuselage $x = 0.38L$, the wing-root fairings represented considerable modification of the basic cross-sections for the slender UTN7-configuration.

Once the cross-sections were defined, a mandrel of balsa and a female mold of RTV were made prior to casting the actual plastic models. The models, which were made of plastic casting resin, were instrumented with pressure taps as shown in Figs. 3 and 4.

Testing Program

The free-stream Mach number for the range of test conditions considered was 4.97 ± 0.02 . The stagnation pressure range was $1.62 \times 10^6 \text{ N/m}^2$ (235 psia) to $2.86 \times 10^6 \text{ N/m}^2$ (415 psia) with a maximum fluctuation during a run of $\pm 13.78 \times 10^3 \text{ N/m}^2$ (± 2 psi). The stagnation temperature range was 294°K (530°R) to 311°K (560°R). The resulting free-stream Reynolds number per cm range was 0.493×10^6 to 0.854×10^6 (15×10^6 to 26×10^6 per foot). Based on the model effective length, this Reynolds number range corresponds to a model Reynolds number range of approximately 8×10^6 to 13×10^6 .

The angle-of-attack range was from 20° to 45° . By using double exposure photographs of the model before and during the run, it was found that wind loads increased the angle of attack during the run by approximately 0.5° .

Data taken consisted of photographs of oil flow patterns, schlieren photographs, and model surface pressures. Actual run schedules are presented in Table 1.

DISCUSSION OF RESULTS

As noted previously, photographs of the surface oil-flow patterns, schlieren photographs, and measurements of the surface pressure were obtained to help define the flow field. The discussion of results will be divided into the type of data obtained. A phenomenological model of the resultant flow-field will be discussed.

Surface Oil-Flow Patterns

Photographs of the surface oil-flow patterns were obtained for both configurations over the entire angle-of-attack range. All the oil-flow patterns presented in this paper were obtained at a nominal free-stream Reynolds number based on effective model length of 9.5×10^6 . Since the oil-flow photographs were taken with a hand-held camera while the tests were in progress, the camera distance and the angle relative to the model varied from picture to picture. The photographs have been trimmed to compensate to a degree for this variation.

The lee-surface oil-flow pattern and the top-view schlieren for the UTN7 at an alpha of 30° are combined in Fig. 5. Both the jowl-generated shock-wave (which produced the perturbations in heat transfer and in surface pressure for the windward surface, ref. 6) and the canopy-generated shock-wave (which produced the perturbations in heat transfer and in surface pressure for the canopy windshield, ref. 7) are evident. The oil-flow pattern for the nose region is that for a free-vortex-layer type of separation, as described in the Introduction. The initial separation from the plane of symmetry appears (in this photograph) to take place at a singular point, as described by Der (ref. 1). However, the oil-flow pattern from a repeat run at this condition did not exhibit an oil accumulation

in the plane-of-symmetry, although it was essentially the same otherwise. This second separation pattern corresponds most nearly to that observed by Stetson (ref. 3), which is illustrated in Fig. 1b. The difference between the two separation patterns occurred because the pretest oil applications differed slightly. It should be remembered that the information obtained from oil-flow data depends on the skill of the experimentalist, as well as the physical character of the oil, e.g., viscosity. The fact that a shearing force has removed the oil from the leeward plane-of-symmetry (downstream of the initial separation) indicates a strong axial flow-component in this region. The accumulation of oil at $x = 0.25L$ indicates that this axial flow separates from the canopy surface. Oil flowing from the side of the canopy toward the low-pressure region just aft of the axial separation leaves a spiral trace. Thus, the canopy breaks up the original separation pattern, creating a new vortical shear-layer.

$\alpha = 20^\circ$. - The oil-flow patterns for an alpha of 20° are presented in Fig. 6 for the two configurations. An (almost linear) accumulation of oil along the leeward ridge of the UTN2 (i.e., the tangency between the linear fall-away side and the elliptic cap in Fig. 3) indicates the vanishing of the circumferential shear component. As indicated by lengthy oil-streaks around the canopy, there remains a strong axial-flow component leeward of this "separation" line. Note also, the "feather" pattern on the lateral surface of the UTN2 below the canopy. At this low alpha, flow from the windward keel apparently separates at the windward chine. The flow on the lateral surface responds to the resultant low pressures, producing the extensive feather pattern. Feather patterns in the vicinity of the wing-root leading edge have been observed by other investigators, e.g., ref. 8.

Whereas the canopy has no apparent effect on the separation line of the UTN2, there is a marked perturbation in the "separation" contour in the vicinity of the UTN7 canopy. The interaction is believed to be the result of the confluence of the circumferential flow and the axial flow. Note also that there is no feather pattern in the lateral-surface oil-flow patterns of the UTN7. Although the University models did not include wings, the wing-root fairings (or jowls) were represented in the models. The jowls, which are evident in the cross-sections of Fig. 4, did not appear to affect the oil-flow pattern on the lateral surface of the UTN7.

Near the windward chines, the surface streamlines are almost perpendicular to the model axis for both configurations.

$\alpha = 25^\circ$. - The side-view oil-flow patterns for an alpha of 25° are presented in Fig. 7. Again, there is an almost linear accumulation of oil along the leeward ridge of the UTN2. There are lengthy oil-streaks around the canopy indicating a strong axial flow-component leeward of this "separation" line. However, the oil accumulates (albeit erratically) on the aft surface of the canopy indicating the "onset" for the UTN2 of the secondary separation noted in Fig. 5. (There is a similar oil accumulation for the UTN7 even at an alpha of 20°). At this alpha, the feather pattern near the wing-root junction (or jowls) of the UTN2 affects only a limited region.

The canopy-induced perturbation in the separation contour for the UTN7 is not quite as extensive for an alpha of 25° as for an alpha of 20° . However, the oil accumulation location in the leeward pitch-plane is further upstream of the canopy than was the case for an alpha of 20° .

$\alpha = 30^\circ$. - The side-view oil-flow patterns for the two configurations are presented in Fig. 8; the top-view photographs in Fig. 9. The oil-streak lines on the lateral surface are roughly perpendicular to the model axis for both configurations. No feather patterns were evident for either configuration. A linear accumulation of oil is again evident along the leeward ridge of the UTN2. The separation line is perturbed in the vicinity of the UTN7 canopy, although the extent of the perturbation continues to decrease with alpha. The top-view oil-flow pattern indicates that the initial separation is of the free-vortex-layer type. The general features of the pattern have been discussed in Fig. 5 and will not be repeated here.

Comparing the side-view pattern for the UTN7 at an alpha of 30° with those for the lower alphas, it is evident that the initial separation location near the plane of symmetry moves upstream with alpha. Not only does the separation on the cowling move upstream with alpha, but the extent of the canopy-induced perturbation in leeward pitch-plane heating moves upstream with alpha (ref. 7). Comparing the top-view oil-flow patterns for the two configurations at an alpha of 30° indicates that separation occurs further upstream for the UTN2 than for the UTN7. Not only does the separation pattern extend further upstream for the UTN2, but the extent of the heating perturbation at this alpha is also further upstream for the UTN2 (ref. 6).

In the side-view photographs, an oil accumulation is evident on the aft surface of the canopy for both configurations. The top-view photograph of the accumulation due to the secondary separation even more clearly exhibits bubble-type characteristics. However, the oil flowing from the side of the canopy toward the low-pressure region just aft of the axial separa-

tion location leaves a spiral trace. Thus, the canopy breaks up the original pattern creating a new vortical shear layer. Downstream attachment of the vortical patterns was not evident in the oil-flow patterns from the UT SWT tests. However, for the AEDC tests of these geometries, it was noted (ref. 7): "Downstream of the canopy, a viscous mechanism has brushed the oil in the vicinity of the plane-of-symmetry. Although the oil-flow pattern does not exhibit the 'Featherlike' characteristics described by the researchers at the Langley Research Center, the vortex is assumed to be the governing viscous mechanism for the present configurations also." The difference in the present oil-flow patterns downstream of the canopy is attributed either (1) to different oil-flow techniques and oil viscosity or (2) to geometry (since the UT models simulated only the nose region, while the AEDC models represented the entire configuration).

$\alpha = 40^\circ$. - The side-view oil-flow patterns for an alpha of 40° are presented in Fig. 10. Marked differences are evident in the separation patterns at this alpha, the highest for which data were obtained. The separation contour is almost linear for both configurations. Thus, the canopy-induced perturbation evident at the lower alphas for the UTN7 is no longer present. The alpha-dependence of the canopy-windshield pressure also changes markedly at this alpha (ref. 6). The oil-flow patterns in the separated region do not exhibit the length streak lines evident at the lower alphas.

Another difference between the oil-flow patterns at an alpha of 40° and those at the lower alphas occurs in the vicinity of the oil accumulation on the lateral surface of the model. At the lower alphas, the streak lines turn parallel to the separation line indicating that the shear does not vanish (as has been noted previously). However, for an

alpha of 40° , the streak lines appear to approach the separation line from a perpendicular direction (except near the base of the model). Thus, the shear goes to zero in this region and separation from the lateral surface does not produce the helical vortices shown in Fig. 1.

Schlieren Photographs

Presented in Fig. 11 is a "typical" side-view schlieren photograph, which is for the UTN7 at an alpha of 30° . The schlieren photograph gives further evidence of the flow mechanisms discussed previously. The free-vortex type of separation appears as a relatively thick shear-layer ahead of the canopy. A shock wave is generated when the flow, which has a strong axial-flow component, encounters the windshield. The secondary flow separation, which originates at $x = 0.25L$ and appears as the wake shear-layer, is consistent with the oil-flow patterns.

$\alpha = 20^\circ$. - The schlieren photographs for the two configurations at an alpha of 20° are compared in Fig. 12. The viscous flow on the leeward surface upstream of the canopy appears as a relatively thin, uniform-intensity trace in the photographs. Furthermore, at this angle of attack, the pressures on the cowling did not exhibit the Reynolds number dependence which is associated with flow separation (ref. 6). These data indicate that flow does not separate from the cowling upstream of the canopy (where the pitch-plane surface element is parallel to the free-stream direction).

Recall, however, that the oil-flow patterns clearly exhibit a "separation" line, i.e., an oil accumulation which indicates the vanishing of the circumferential shear component. But, as noted previously, the lengthy oil streaks around the canopy indicate that there remains a strong axial-

flow component leeward of the "separation" line. Thus, it appears that, while the transverse pressure gradient due to crossflow causes the circumferential flow to break away from the surface, the viscous flow remains attached to the leeward, cowling surface. The separation of the circumferential flow creates a free shear surface bounding the leeward flow. For the present configurations, the leeward flow separates from the aft surface of the canopy.

$\alpha = 30^\circ$. - For an alpha of 30° , the leeward viscous flow appears as a much thicker trace in the schlieren photographs of Fig. 13 than was the case at an alpha of 20° . Also note that the photographic trace of the shear layer exhibits a dark region near the surface just upstream of the windshield. This varying intensity of the relatively thick shear-layer is consistent with the free-vortex layer indicated by the oil flow patterns (Figs. 8 and 9). Furthermore, for angles-of-attack of 30° or greater, the leeward surface-pressures decreased as the Reynolds number increased, which was indicative of separated flow.

The canopy-generated shock wave remains very close to the windshield surface both for alpha of 20° and of 30° . For an alpha of 20° , the canopy-induced perturbation does not affect the heat transfer to the thermocouples upstream of the canopy. At an alpha of 30° , perturbations are evident at thermocouples upstream of the canopy. The extent and the magnitude (never severe) of the heating perturbations are configuration dependent (ref. 6).

The leeward flow-pattern for an alpha of 30° , therefore, contains a free-vortex-layer type of separation from the nose region and a canopy-generated shock-wave which has only a slight effect on the upstream flow.

$\alpha = 40^\circ$. - The schlieren photographs for an alpha of 40° are presented in Figs. 14 and 15 for the UTN2 and for the UTN7, respectively. To provide all the flow-field features which were evident in the original photographs, sketches of the photographic flow pattern are included. Near the apex, the viscous layer is very thick, much thicker than at an alpha of 30° . While there is a single canopy-generated shock-wave at the lower alphas, two shock waves are evident in the schlieren photographs for an alpha of 40° . The interaction between the outer shock wave (segment) and the viscous flow produces perturbations in the heat transfer well upstream of the canopy windshield for both configurations (ref. 7). The oil-flow patterns exhibit an accumulation of oil upstream of the canopy on the cowling away from the plane of symmetry. The accumulation of oil indicates separation in this region and, therefore, is consistent with the very thick shear layer. However, a longitudinal oil-streak line appears near the plane of symmetry. Also note that there is a shock-wave trace at the canopy windshield. Furthermore, the heat transfer to the canopy windshield remains high, indicating that there is a strong axial flow-component near the pitch plane.

Thus, the leeward flow-pattern appears to be different than the vortical free-vortex-layer separation observed at 30° . At an alpha of 40° , flow appears to separate "cleanly" from the lateral surface. The separation contour is almost linear, with no canopy influence even for the UTN7. In the pitch plane, flow accelerates from the windward stagnation point into the low-pressure region on the leeward cowling. A shock is generated when this axial flow encounters the canopy. The majority of the leeward flow appears to be a separated flow, which is dominated by an interaction between a canopy-generated shock-wave and the viscous flow. The inter-

action affects the pitch-plane heating, causing increases well upstream of the windshield.

Surface-Pressure Data

Pressure data from the current test program have been presented elsewhere, specifically, refs. 6 and 7. The reader is referred to these references for pressure distributions which can be used to help define the flow field. The pressure data for Figs. 16 through 18 are presented to help define the general characteristics of the configurations tested.

Pressures from the leeward plane-of-symmetry are presented in Fig. 16. Pressure measurements from the nose region of the University configurations are compared with measurements made using a slender, sharp cone. Although the measurements on the cowling of the present configurations are significantly higher than the cone pressures, the alpha-dependence is qualitatively similar for all three configurations. The cowling pressures for the present shuttle configurations have been shown to agree with similar measurements for other shuttle orbiter-configurations (see ref. 6). The pressures presented in ref. 6 (which were for $x = 0.08L$) were significantly influenced by the shock: viscous-flow interaction at the higher alphas. However, the pressures presented in Fig. 16a are for orifices sufficiently upstream that they are apparently unaffected by the shock: viscous-flow interaction.

The pressures at an orifice downstream of the canopy are presented in Fig. 16b as a function of alpha for both configurations. The alpha-dependence of the data for the wingless, University configurations is similar to that observed by Penland (ref. 10) for right-circular cylinders.

Pressure distributions from the leeward pitch-plane are presented for an alpha of 20° in Fig. 17 for the University shuttle-configurations (which represented only the nose region), a Langley entry configuration (which had no canopy), and an NYU entry configuration (which had no canopy) and a slab delta-wing configuration. Upstream of the canopy-induced perturbations ($x < 0.16L$), the pressures for the various shuttle configurations are in approximate agreement. The pressure differences are attributed to the differences in geometry, i.e., cross-sections, planforms, and profiles. Downstream of the canopy ($x > 0.36L$) the pressure data for the wingless, University models are markedly greater than for the winged shuttle configurations. The differences in pressure measurements downstream of the canopy indicate two broad classes of geometry: winged and unwinged configurations. Presented for comparison are the pressures measured in the leeward pitch-plane of a slab delta-wing configuration (ref. 12). The pressures for the slab delta-wing are between the data levels for the two types of configuration, being in better agreement with the data for the winged configuration.

Pressure distributions from the leeward pitch-plane are presented for an alpha of 40° in Fig. 18 for the University shuttle configurations, a Langley entry configuration, an NYU entry configuration (this particular configuration had a canopy), and a slab delta-wing configuration. However, except near the apex, the pressure data for the present, wingless models are markedly greater than for the winged configurations of refs. 8 and 11. Upstream of the canopy ($x < 0.16L$), the pressures for the University shuttle-configurations are relatively high, because of the canopy-induced perturbations. It has been noted that the shock: viscous-layer interaction

produces a thick shear layer and increased heating well upstream of the canopy (ref. 7). Downstream of the canopy ($x > 0.36L$), the pressures remain relatively high for the current configurations.

The differences between the pressures for the University models and for the other shuttle configurations is attributed to the absence of wings for the University models. Even though the shuttle-configuration pressure data are from the leeward pitch-plane of the fuselage, the magnitudes of the pressures for the winged configurations match closely the data obtained on a slab delta-wing configuration (ref. 12).

Thus, because the University's shuttle models did not include wings (although they did include wing-root fairings), the data downstream of the canopy should not be used for shuttle applications.

CONCLUDING REMARKS

Based on the data and the analyses of the present study, the following conclusions are made for the configurations and the test conditions of this program.

1. Over the angle-of-attack range of the present study, three "distinctive" separation patterns occurred.
 - (a) At an alpha of 20° , the transverse pressure gradient due to crossflow causes the circumferential flow to separate from the lateral surface. However, the flow on the leeward cowl surface appears to be attached.
 - (b) At an alpha of 30° , the separation for the nose region is of the free-vortex-layer type.
 - (c) At an alpha of 40° , separation from the lateral surface does not produce helical vortices. Nevertheless, there remains a strong axial flow component near the leeward pitch plane.
2. The pressure data from the leeward pitch plane of the University shuttle models clearly reflect the absence of the wings.

REFERENCES

1. Der, J., Jr.: "A Study of General Three-Dimensional Boundary-Layer Problems by an Exact Numerical Method", AIAA Journal, Vol. 9, No. 7, July 1971, pp. 1294-1301.
2. Wang, K. C.: "Separation Patterns of Boundary Layer Over an Inclined Body of Revolution," AIAA Journal, Vol. 10, No. 8, August, 1972, pp. 1044-1050.
3. Stetson, K. F.: "Experimental Results of Laminar Boundary Layer Separation on a Slender Cone at Angle of Attack at $M_\infty = 14.2$ " ARL 71-0127, August 1971, Aerospace Research Labs, Wright-Patterson Air Force Base, Ohio.
4. Hefner, J. M., and Whithead, A. H., Jr.: "Lee Side Investigation, Part I - Experimental Lee-Side Heating Studies on a Delta-Wing Orbiter," NASA Space Shuttle Technology Conference, Vol. I - Aerothermodynamics, Configurations, and Flight Mechanics, TM X-2272, April 1971, NASA.
5. Hefner, J. M., and Whitehead, A. H., Jr.: "Lee Side Flow Phenomena on Space Shuttle Configurations at Hypersonic Speeds, Part II - Studies of Lee-Surface Heating at Hypersonic Mach Numbers", Space Shuttle Aerothermodynamics Technology Conference, Vol. II - Heating, TM X-2507, February 1972, NASA.
6. Bertin, J. J., Faria, H. T., Goodrich, W. D., and Martindale, W. R.: "Effect of Nose Geometry on the Aerothermodynamic Environment of Shuttle Entry Configurations", AIAA Paper 73-638, presented at AIAA 6th Fluid and Plasma Dynamics Conference, Palm Springs, July 1973.
7. Bertin, J. J., et al.: "The Effect of Nose Geometry on the Aerothermodynamic Environment of Shuttle Entry Configurations", Aerospace Engineering Report 73001, January 1973, The University of Texas at Austin.
8. Hefner, J. N.: "Lee-Surface Heating and Flow Phenomena on Space Shuttle Orbiters at Large Angles of Attack and Hypersonic Speeds", TN D-7088, November 1972, NASA.
9. Feldhuhn, R. H., Winkelmann, A. E., and Pasiuk, L.: "An Experimental Investigation of the Flow Field Around a Yawed Cone", AIAA Journal, Vol. 9, No. 6, June 1971, pp. 1074-1081.
10. Penland, J. A.: "Aerodynamic Characteristics of a Circular Cylinder at Mach Number 6.86 and Angle of Attack Up to 90° ", RM L54A14, March 1954, NACA.
11. Zakkay, V., Miyazawa, M., and EdSimone, G.: "Reynolds Number and Mach Number Effect on Space Shuttle Configuration", Final Report, NASA Grant NGR-33-016-129, September 1972, New York University.

12. Bertram, M. H., and Everhart, P. E.: "An Experimental Study of the Pressure and Heat Transfer Distribution on a 70° Sweep Slab Delta Wing in Hypersonic Flow", TR R-153, December 1963, NASA.

Table 1. - Nominal run schedule for UT SWT tests.

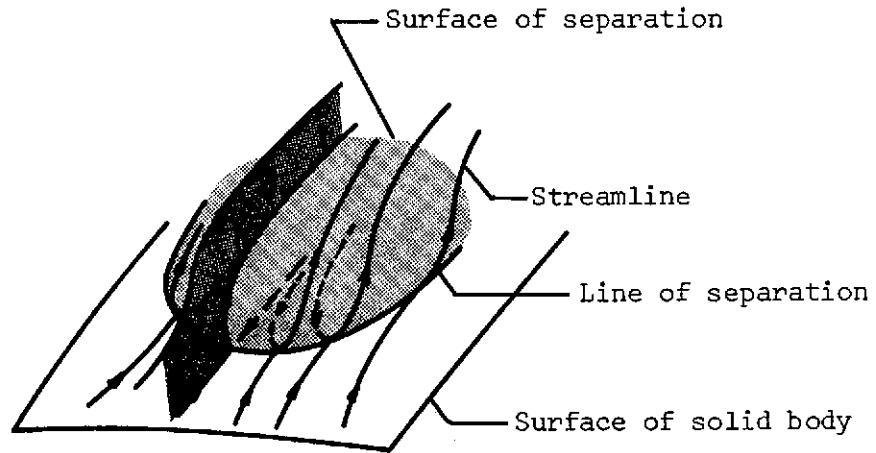
(a) UTN2

α $R_{\infty,L}$ ($\times 10^{-6}$)	20	25	30	40	45
8					
8.6					
9.5	P,S,O	P,S,O	P,S,TS,O,TO	S,O	P
11.					
13					

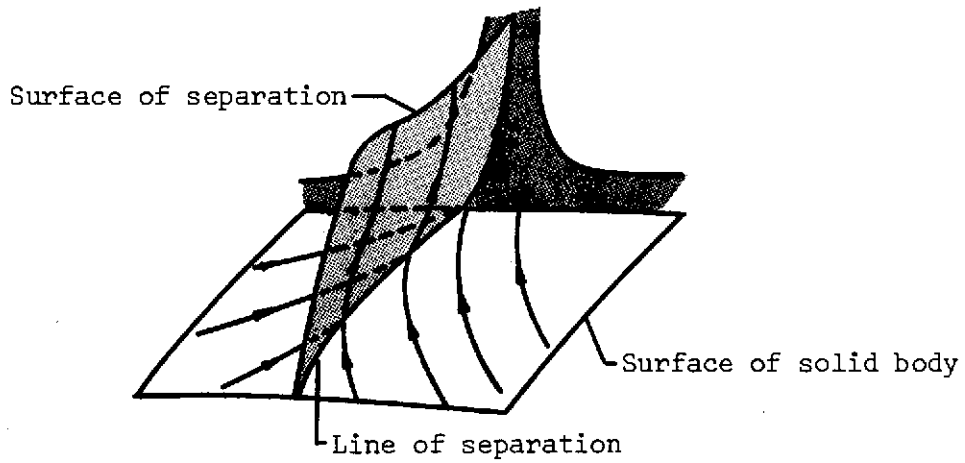
(b) UTN7

α $R_{\infty,L}$ ($\times 10^{-6}$)	20	25	30	40	45
8	P		P		
8.6					
9.5	P,S,O	S,O	P,S,TS,O,TO	P,S,O	
11.	P		P	P	
13	P		P	P	

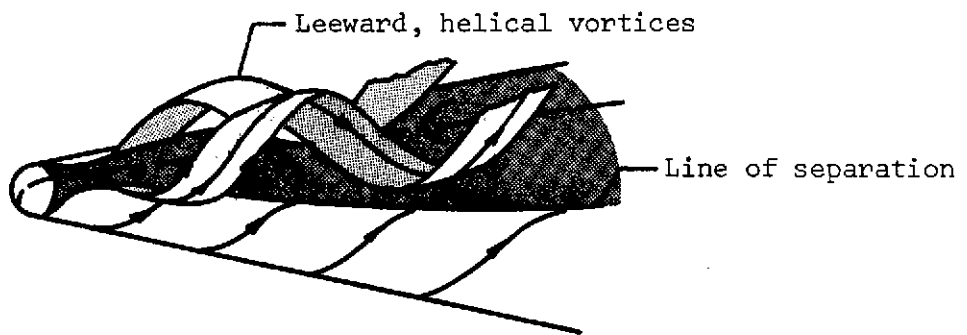
- P - PRESSURE DATA
 S - SIDE VIEW SCHLIEREN PHOTO
 TS - TOP VIEW SCHLIEREN PHOTO
 O - SIDE VIEW OIL FLOW PHOTO
 TO - TOP VIEW OIL FLOW PHOTO



(a) Separation bubble; basic pattern presented by Wang (Ref. 2)



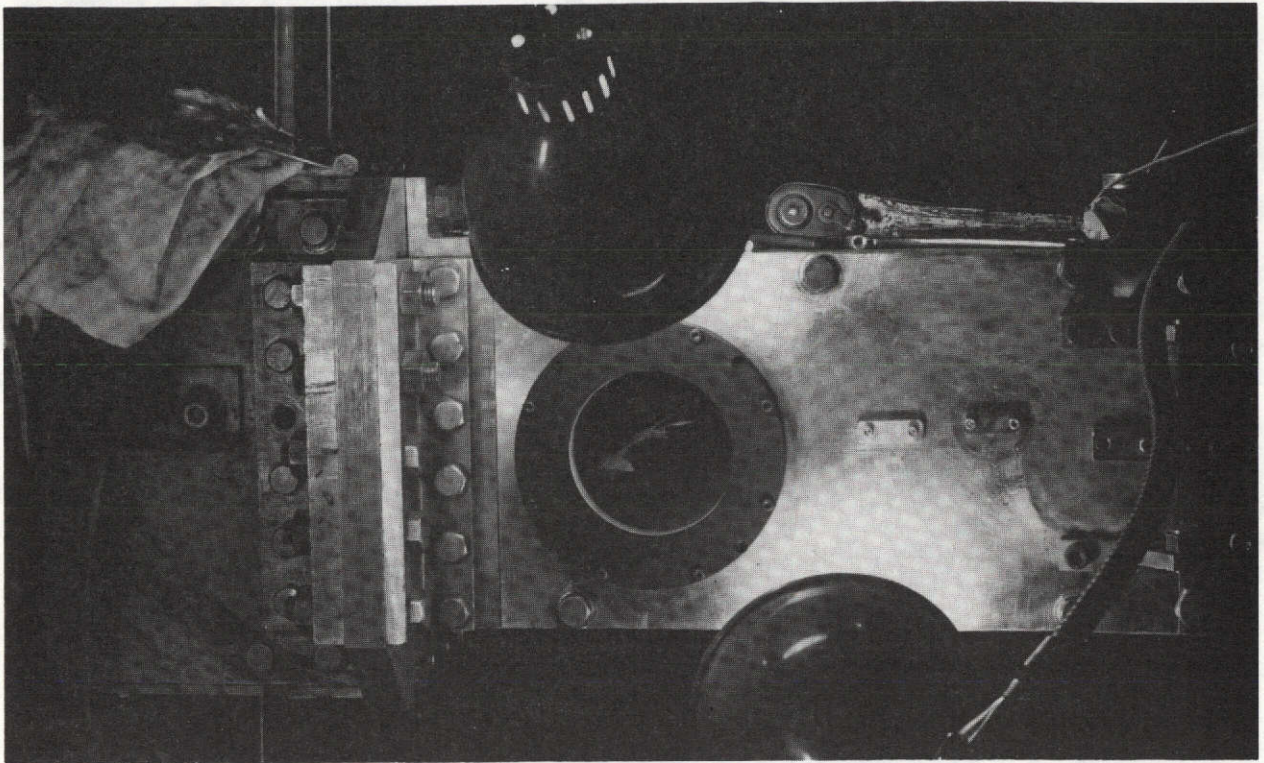
(i) Basic pattern presented by Wang (Ref. 2)



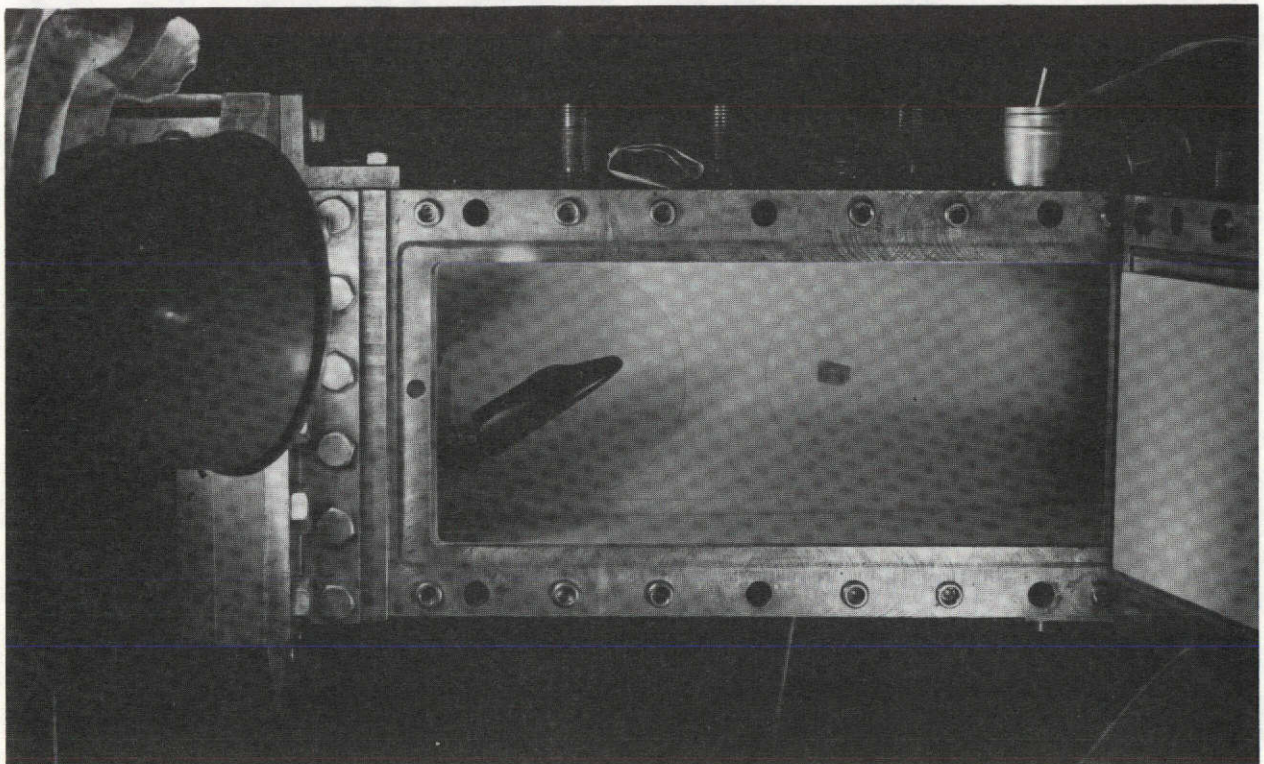
(ii) Model of Stetson (Ref. 3) for a cone

(b) Free-vortex layer

Figure 1. - Sketches of separation patterns.

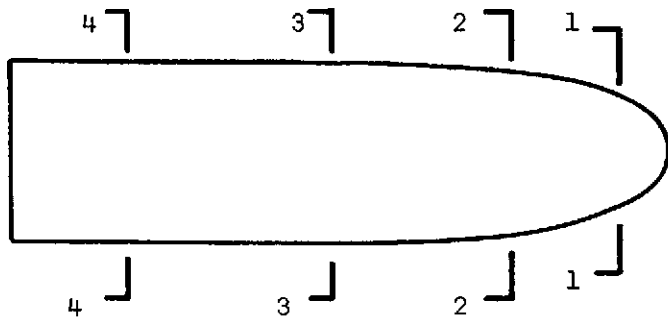


(a) Tunnel door closed

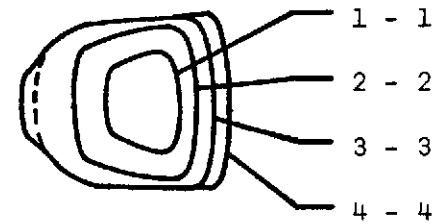


(b) Tunnel door open

Figure 2. - Photographs of typical model in the UT SWT.



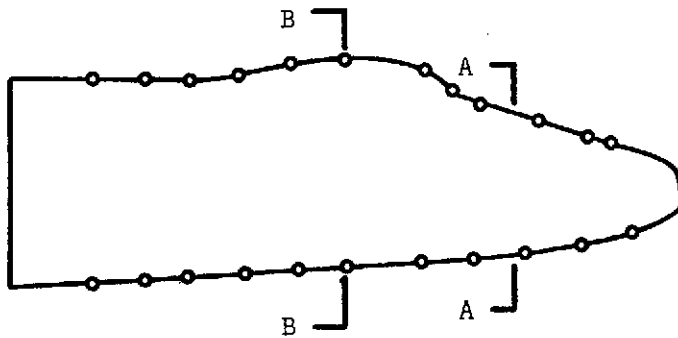
(a) Top view



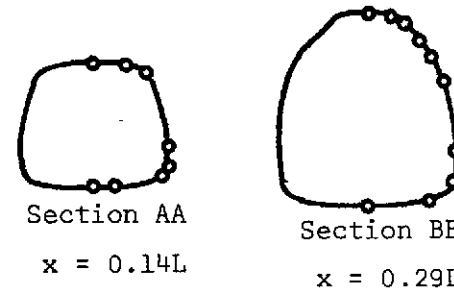
(b) Front-view sections

Model length = 3.45 in.

Effective length = 5.91 in.



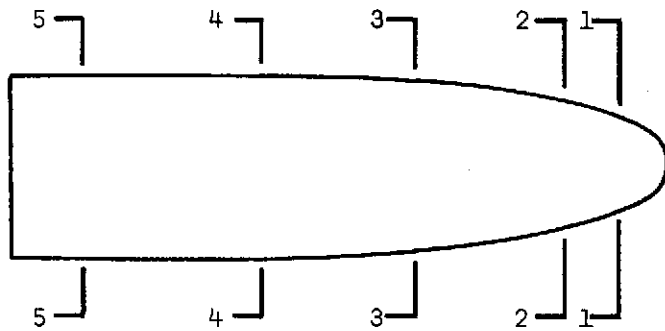
(c) Side view



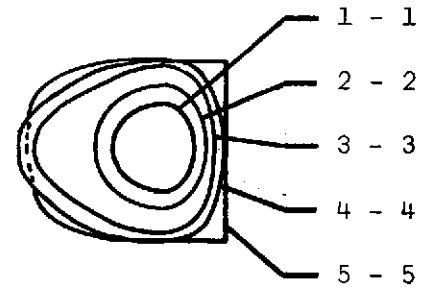
(d) Instrumented cross-sections

Figure 3. - Sketch of UTN2 configuration used in UT SWT indicating pressure-orifice locations.

25



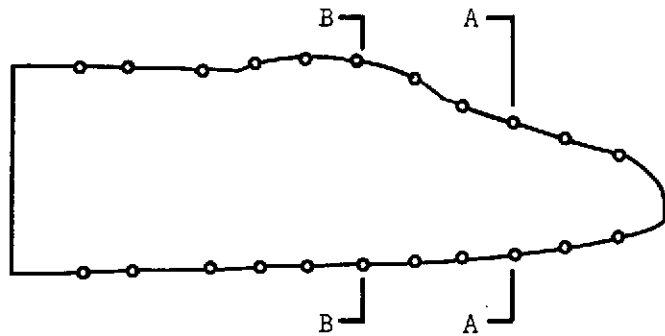
(a) Top view



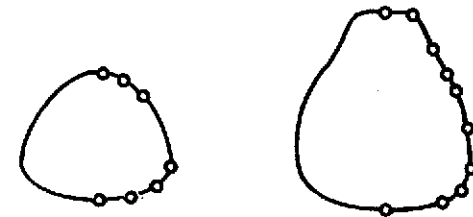
(b) Front-view sections

Model length = 3.4 in.

Effective length = 6.13 in.



(c) Side view



Section AA

$x = 0.12L$

Section BB

$x = 0.26L$

(d) Instrumented cross-sections

Figure 4. - Sketch of UTN7 configuration used in UT SWT indicating pressure-orifice locations.

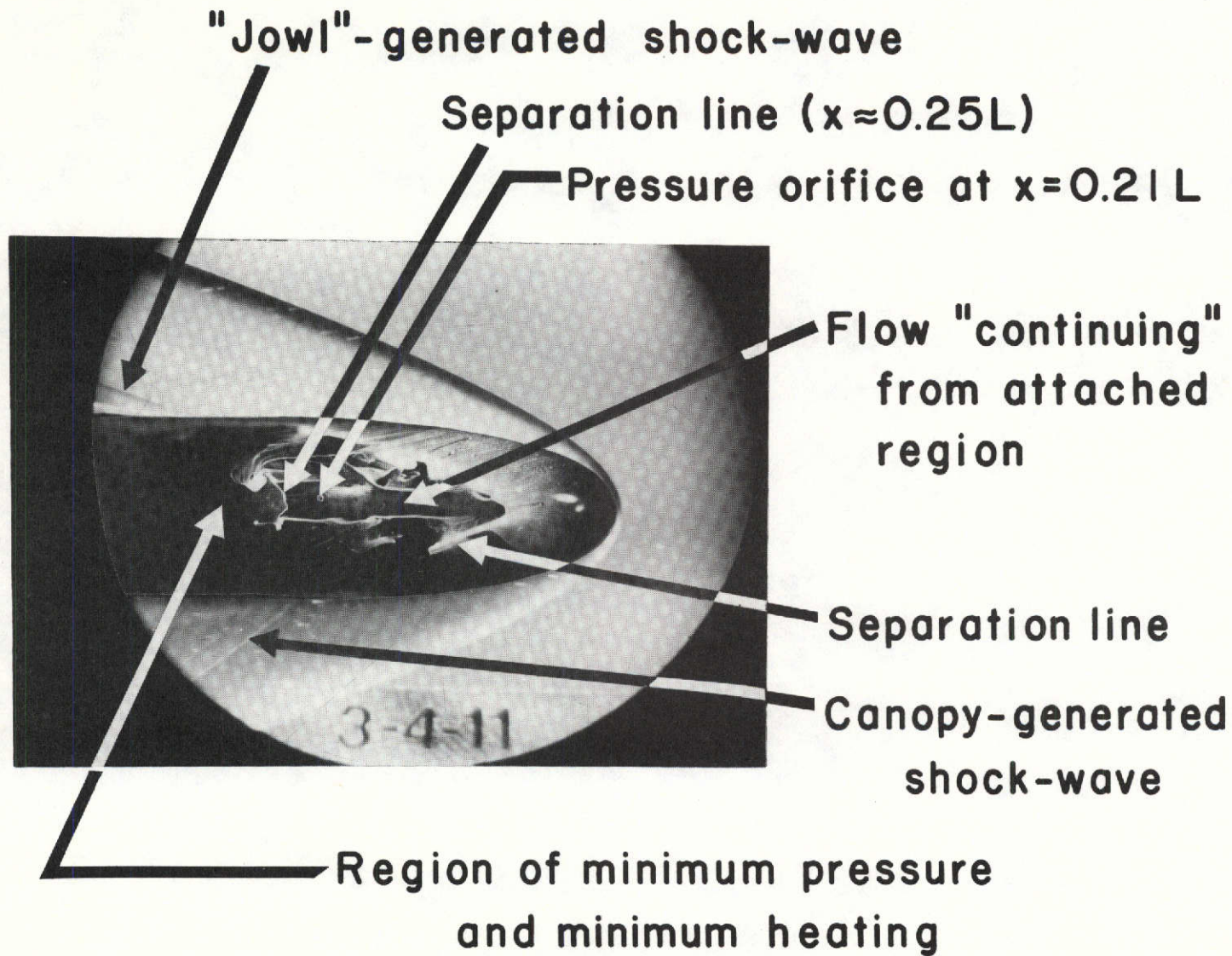
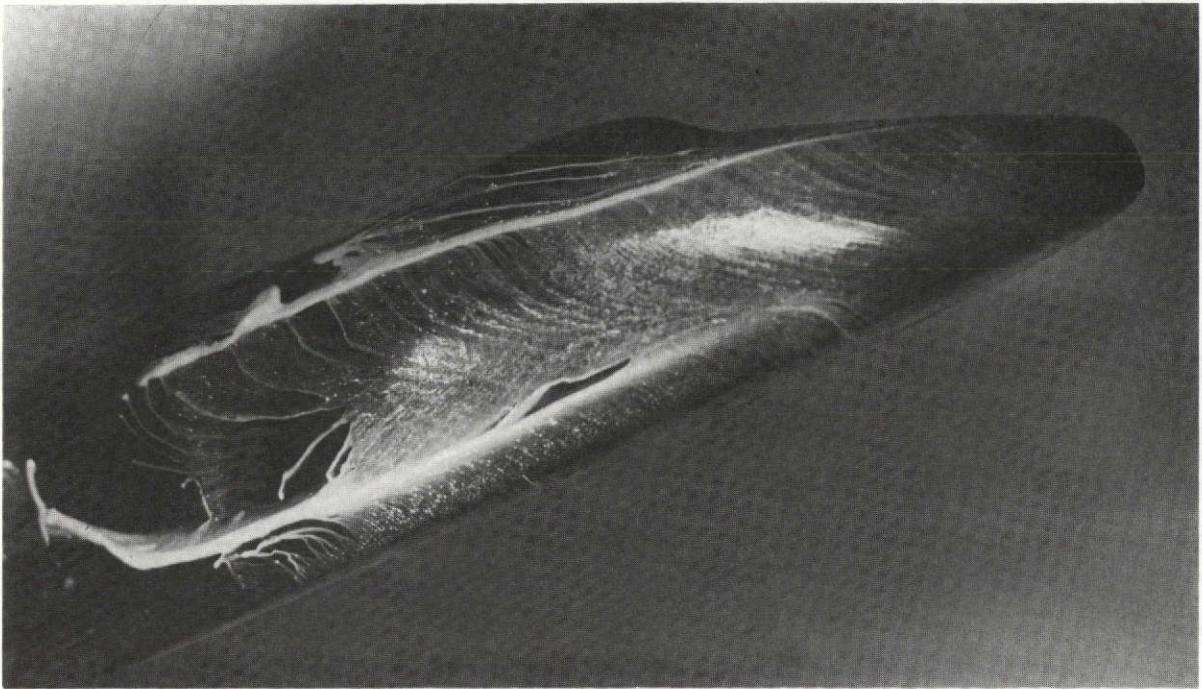
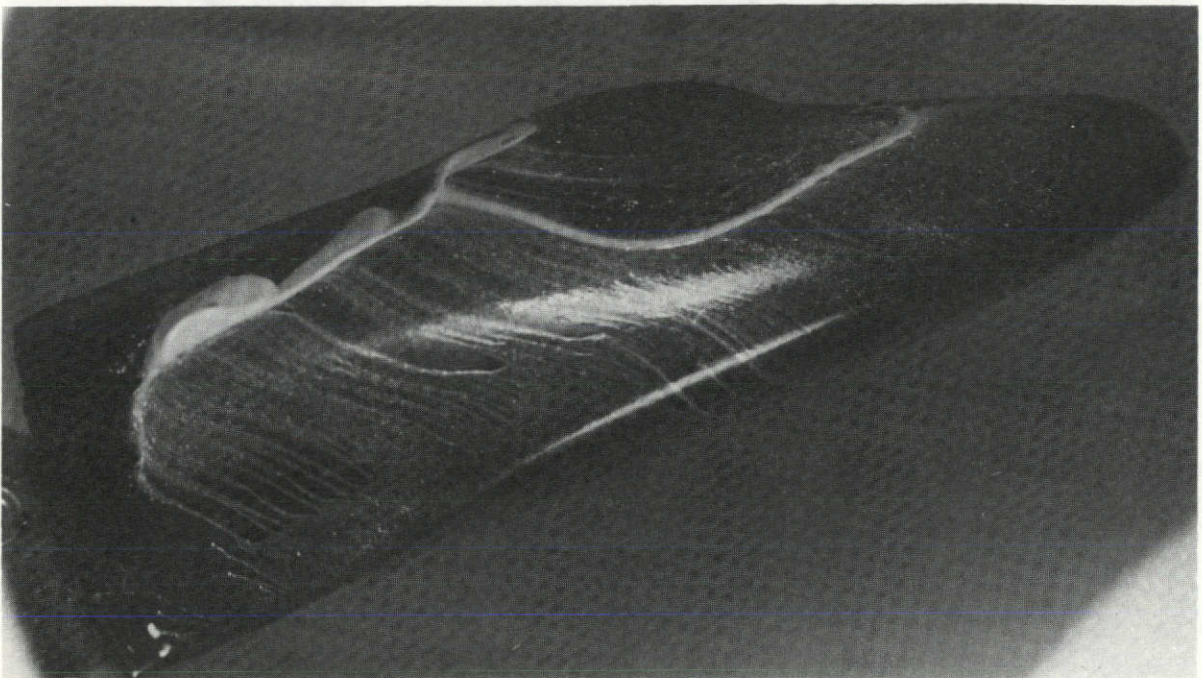


Figure 5. - Flow visualization photograph showing leeward oil-flow pattern and the shock-waves for the UTN7 at an alpha of 30° .

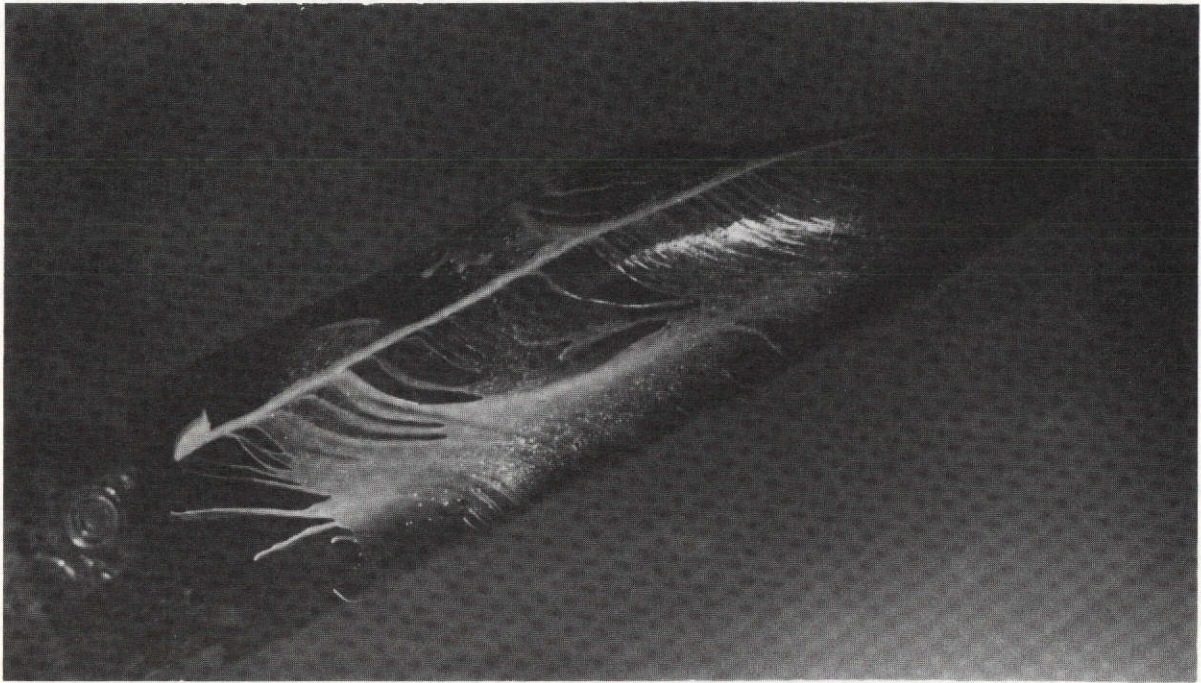


(a) UTN2

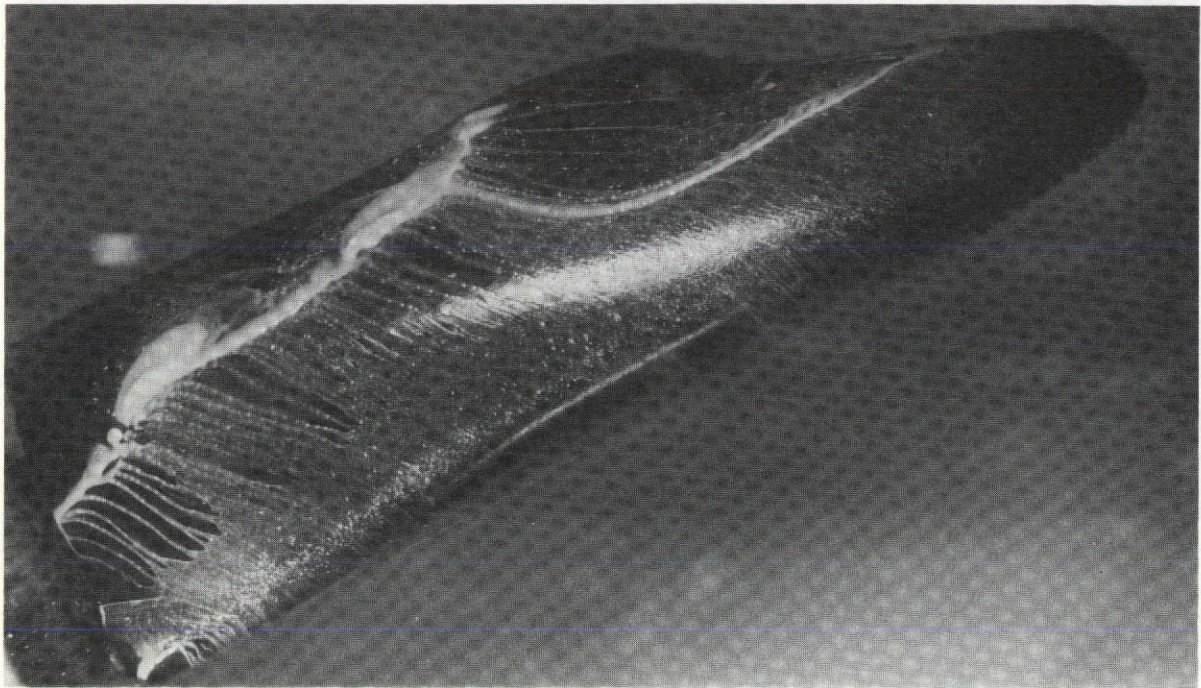


(b) UTN7

Figure 6. - Side view of oil-flow patterns for an alpha of 20°.

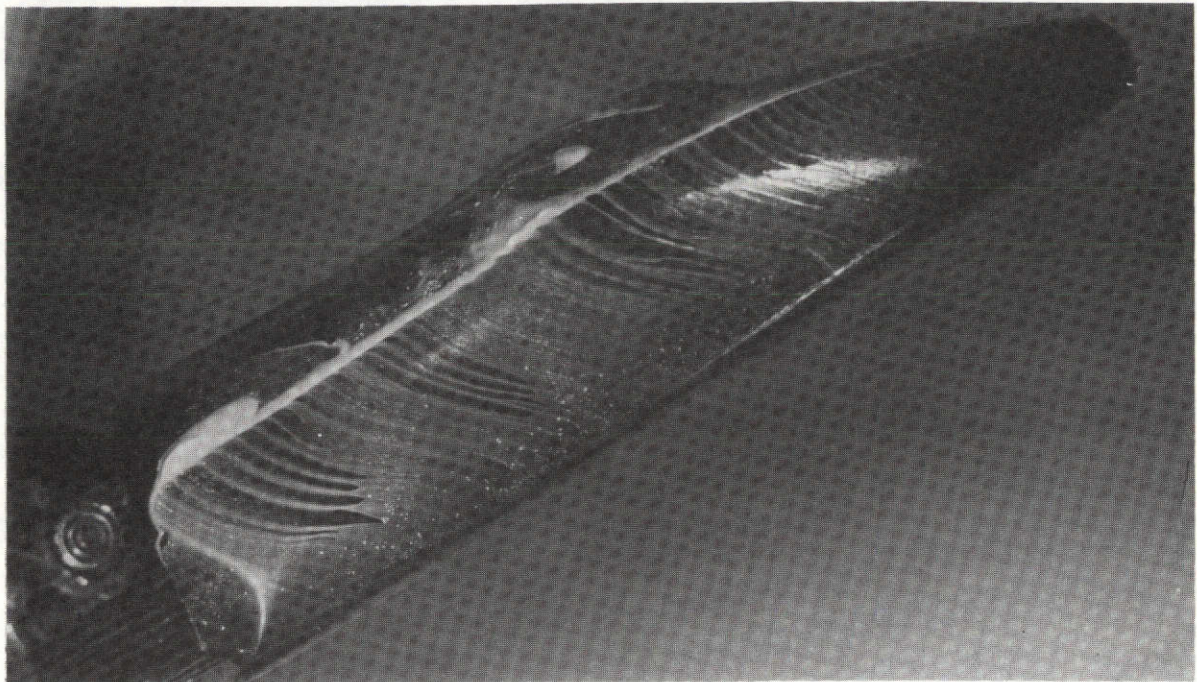


(a) UTN2

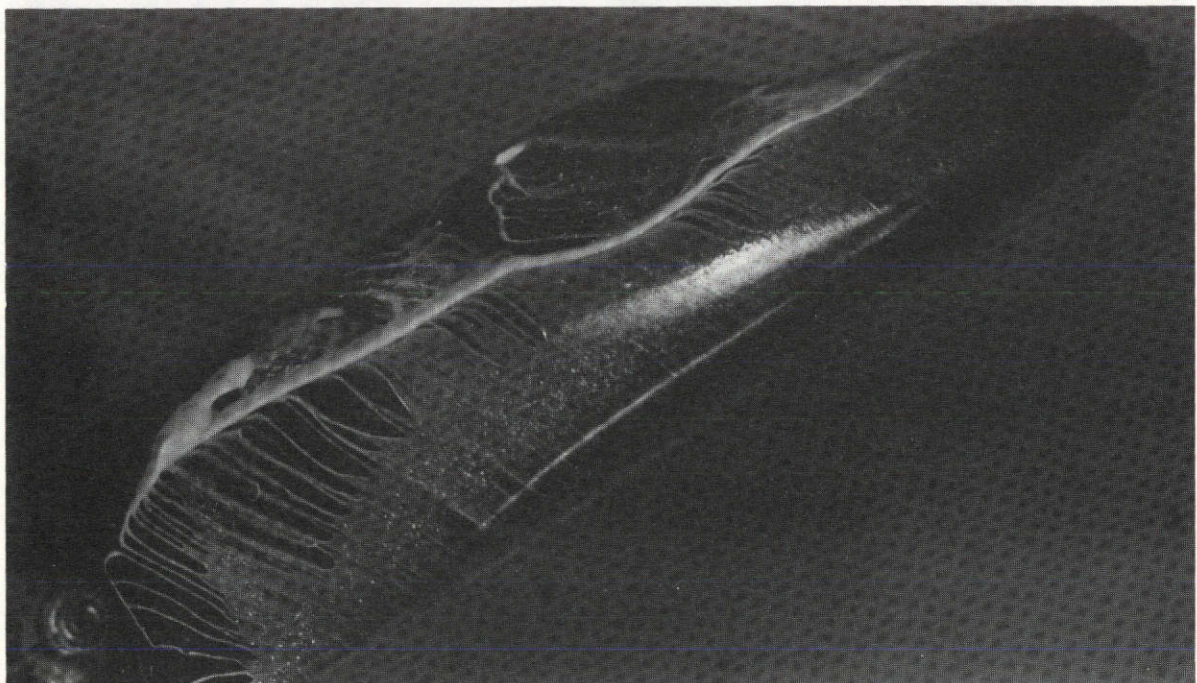


(b) UTN7

Figure 7. - Side view of oil-flow patterns for an alpha of 25° .

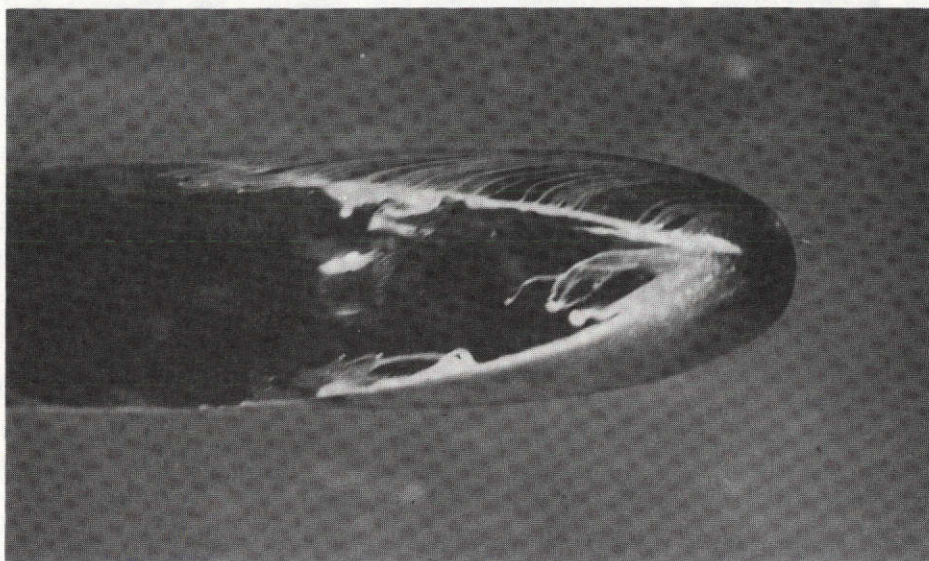


(a) UTN2

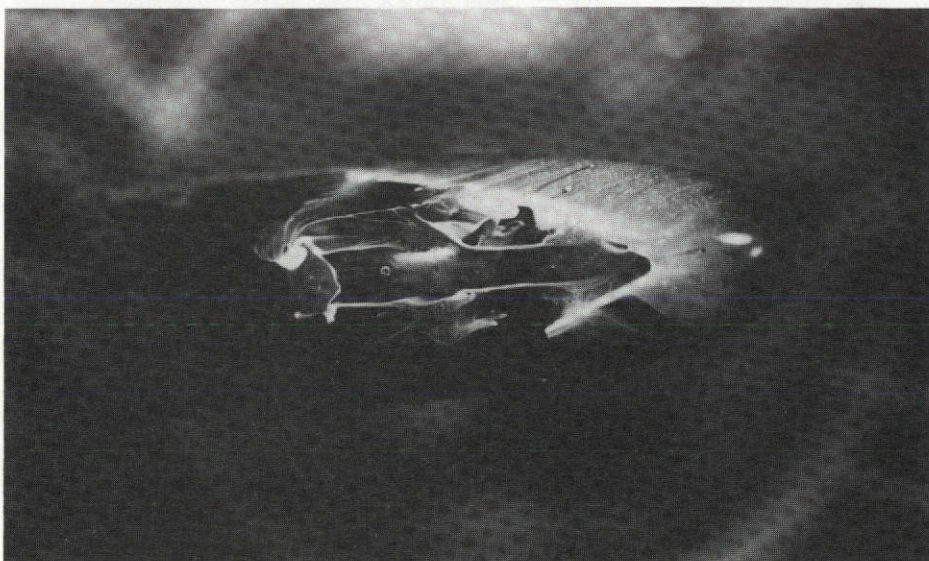


(b) UTN7

Figure 8. - Side view of oil-flow patterns for an alpha of 30°.

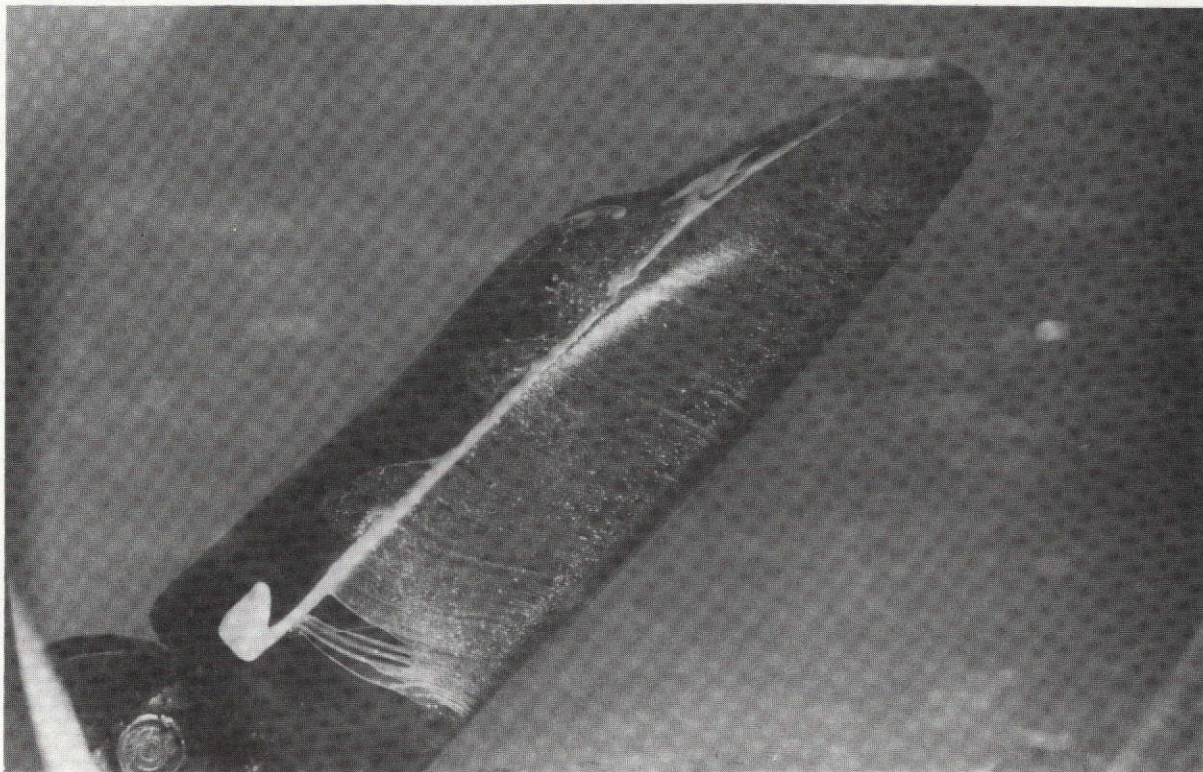


(a) UTN2

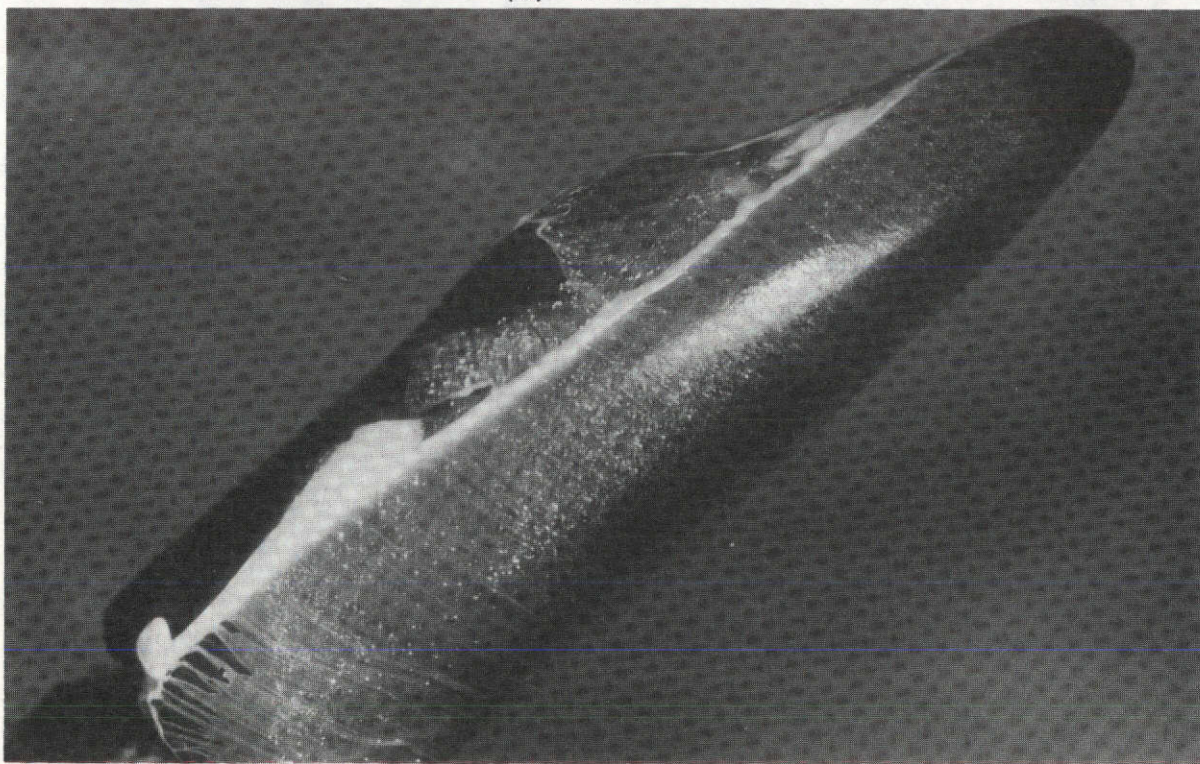


(b) UTN7

Figure 9. - Top (or leeward) view of oil-flow patterns for an alpha of 30° .



(a) UTN2



(b) UTN7

Figure 10. - Side-view of the oil-flow patterns for an alpha of 40° .

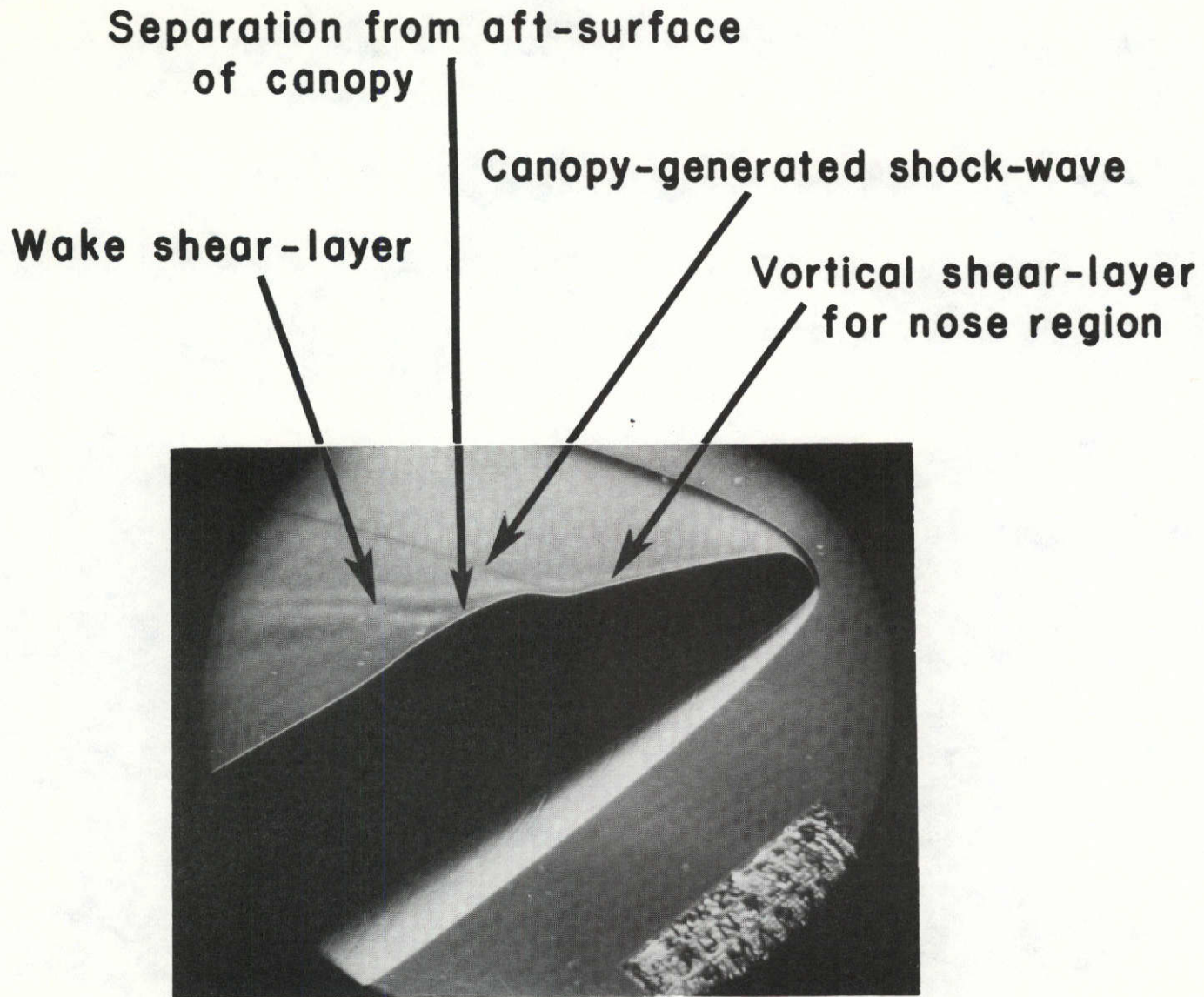
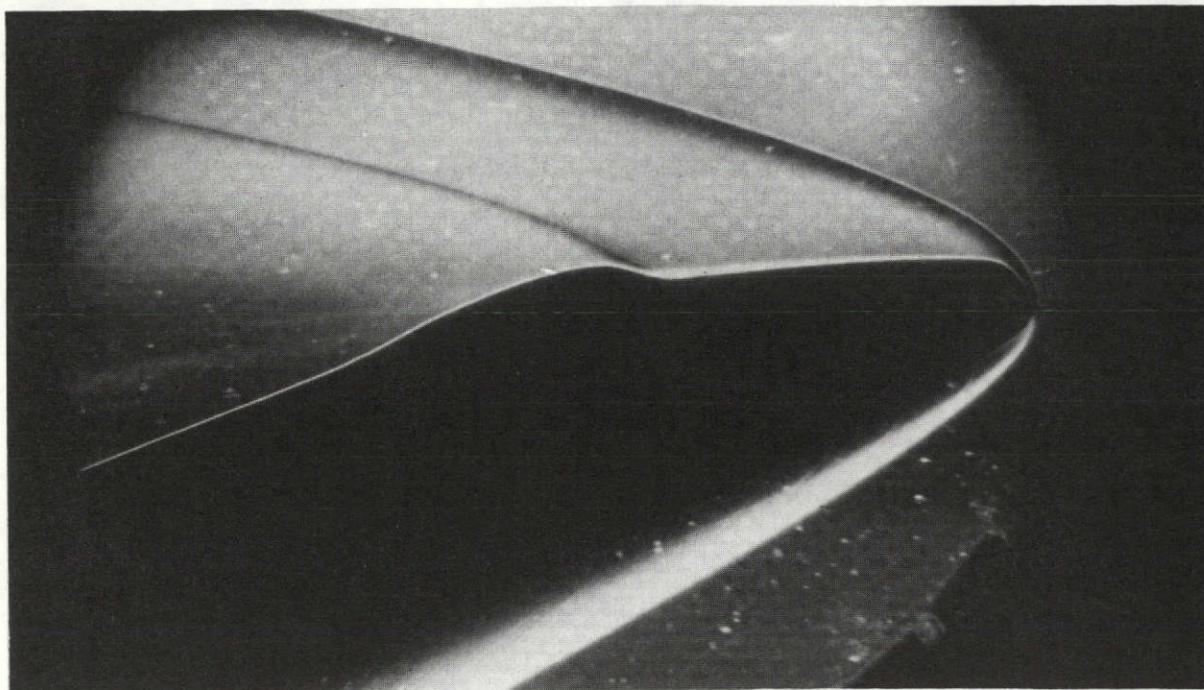
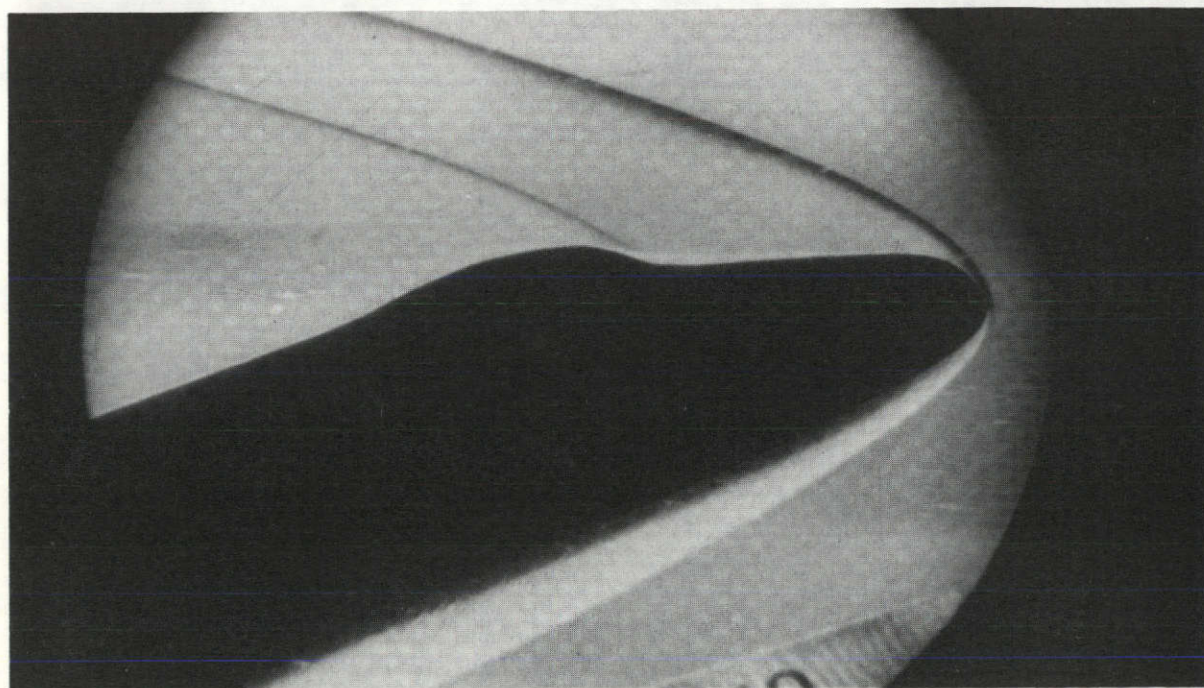


Figure 11. - Side-view schlieren photograph of the UTN2 at an alpha of 30° .

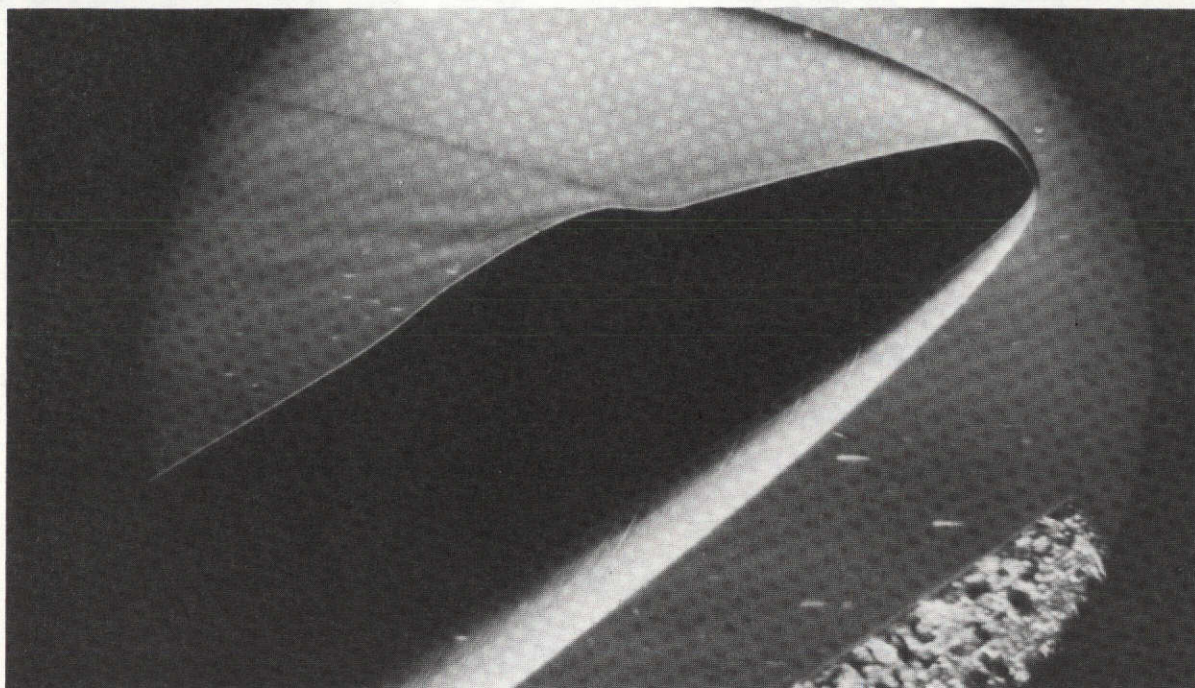


(a) UTN2

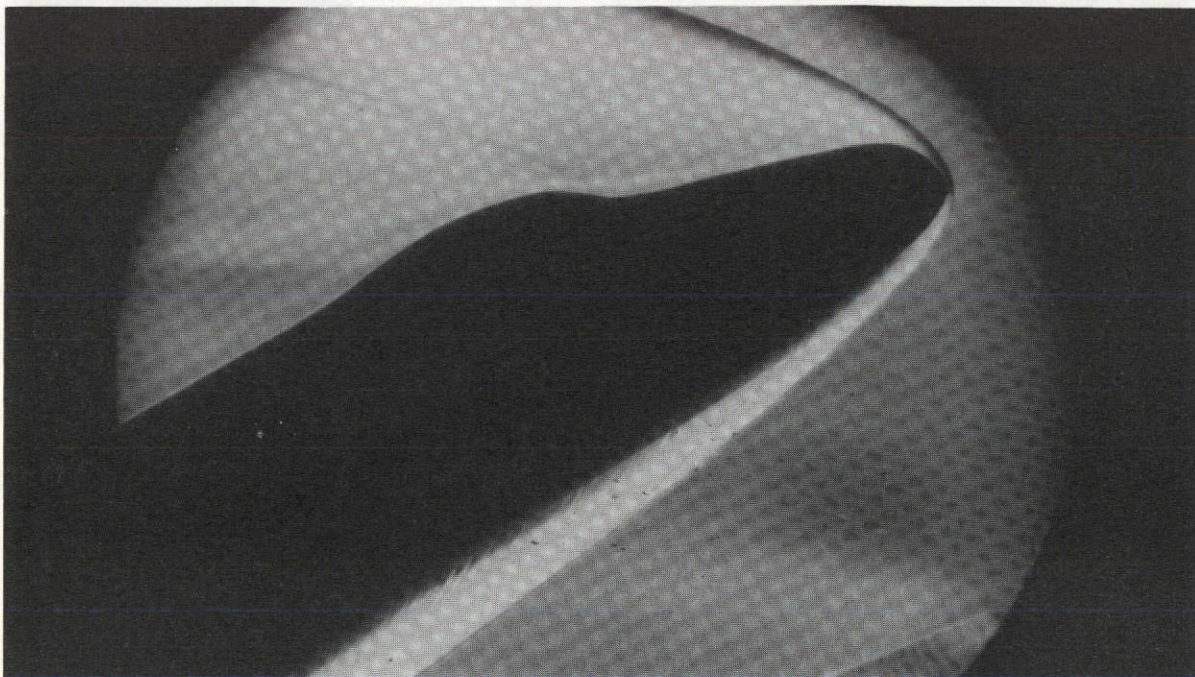


(b) UTN7

Figure 12. - Side-view schlieren photographs for an alpha of 20° .

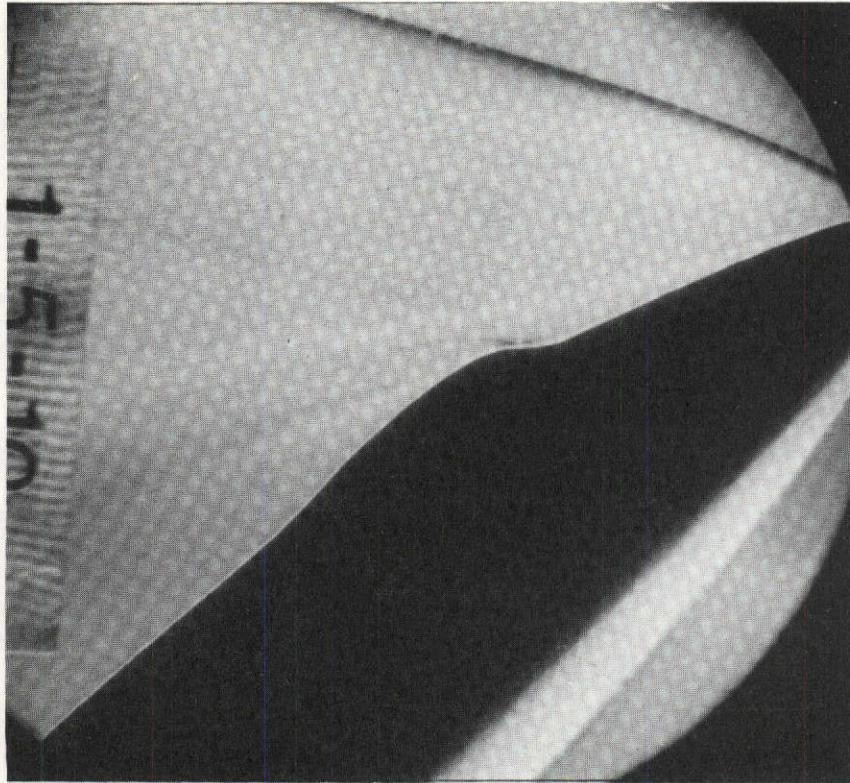


(a) UTN2

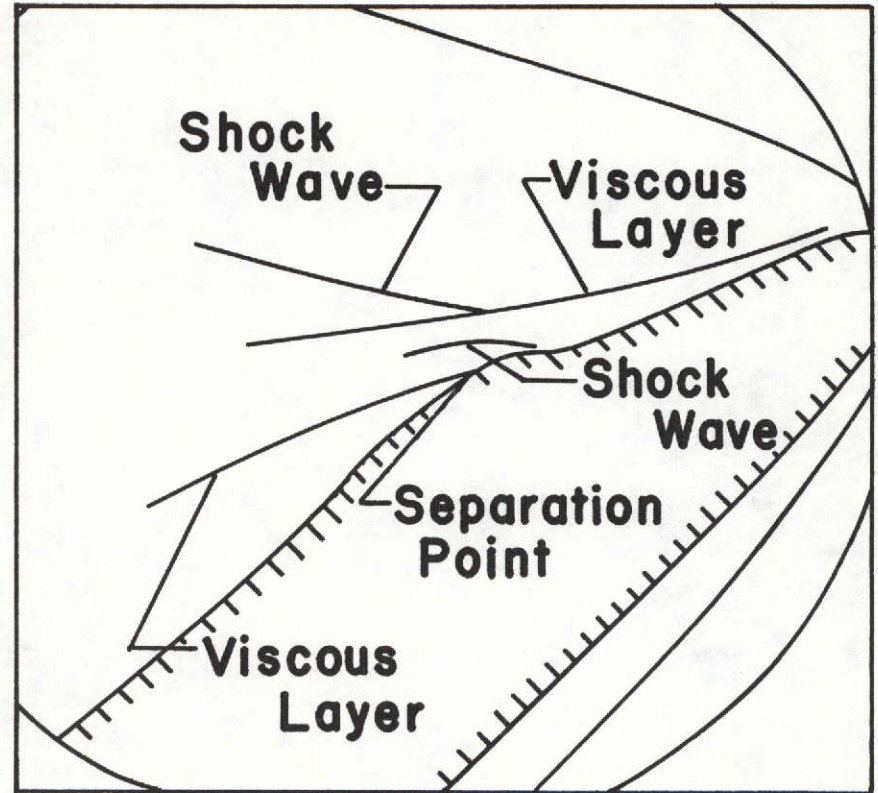


(b) UTN7

Figure 13. - Side-view schlieren photographs for an alpha of 30° .

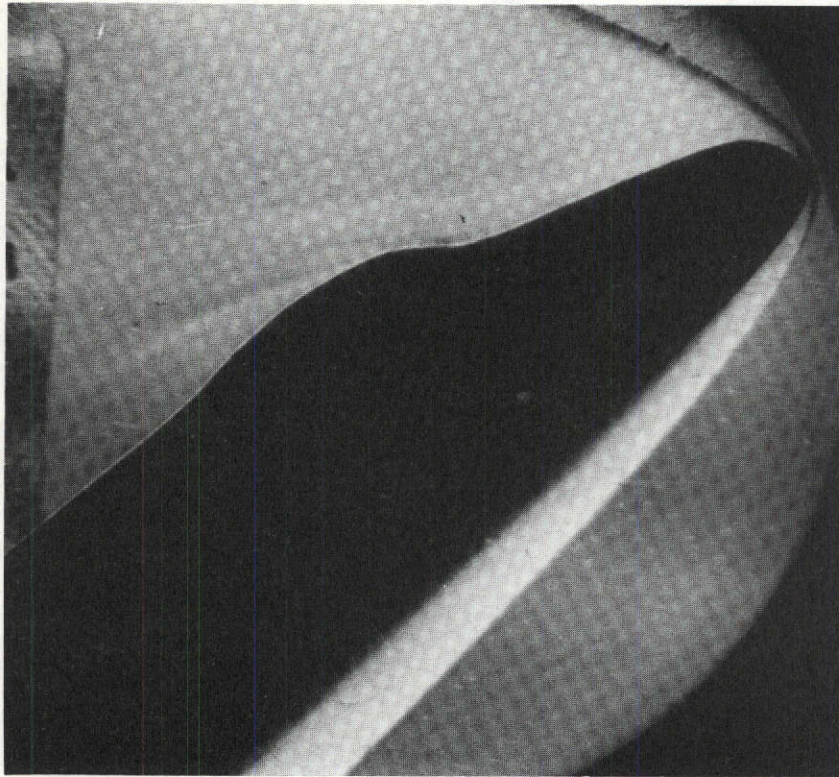


Schlieren Photograph

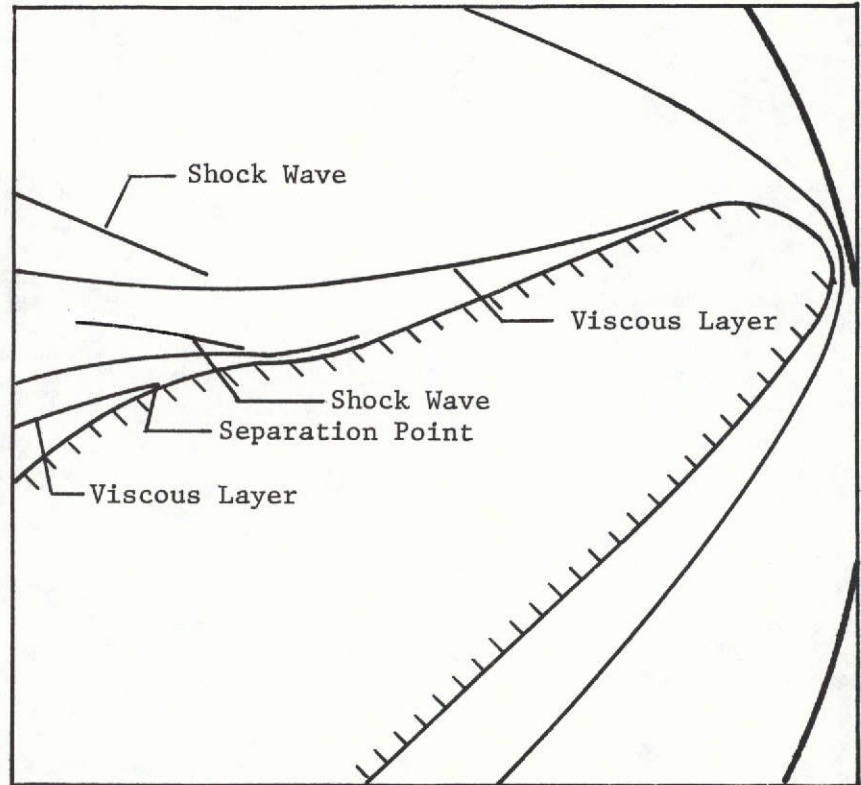


Sketch of Flow Pattern

Figure 14. - Side-view schlieren photograph and illustrative sketch of the flow field for the UTN2 at an alpha of 40° .



Schlieren Photograph



Sketch of Flow Pattern

Figure 15. - Side-view schlieren photograph and illustrative sketch of the flow field for the UTN7 at an alpha of 40° .

△ Sharp cone, 5° semi-vertex angle (Ref. 9)

$$M_\infty = 5, Re_{\infty,L} = 5 \times 10^6$$

○ UTN2, $x = 0.066L$; □ UTN7, $x = 0.042L$

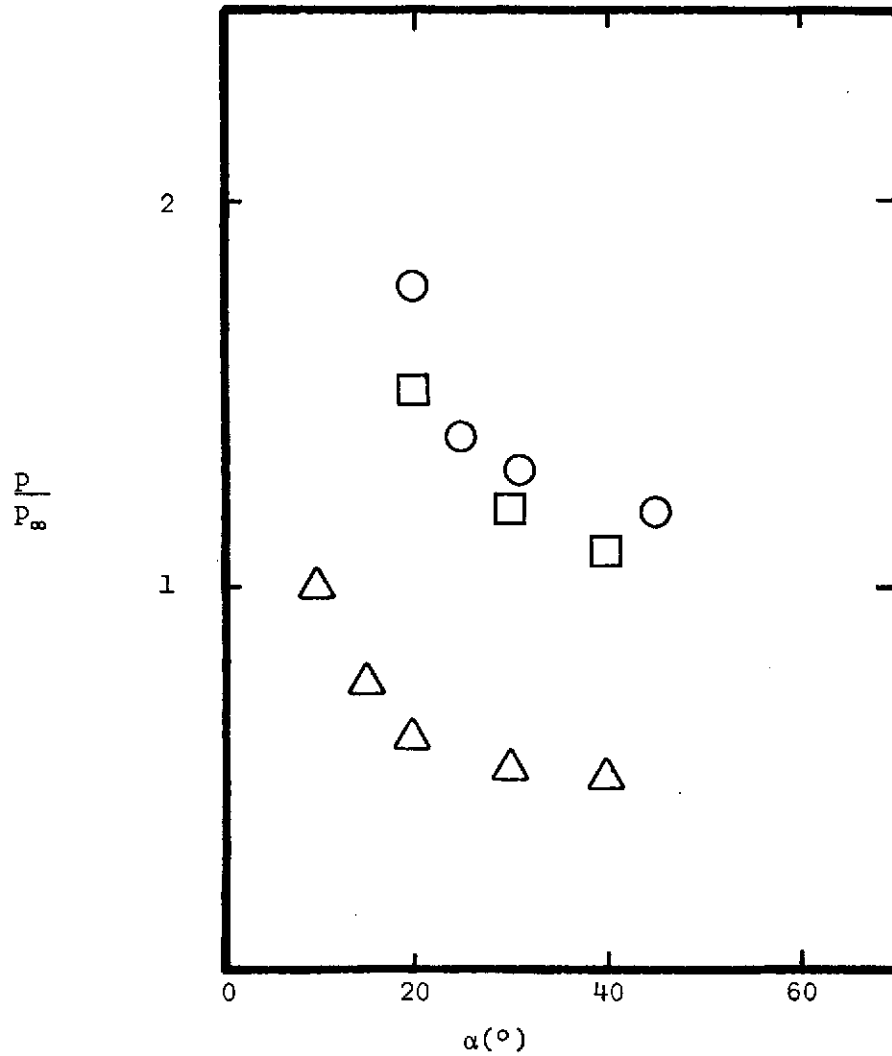
$$M_\infty = 4.97, Re_{\infty,L} = 8 \times 10^6$$

⬡ Circular cylinder (Ref. 10)

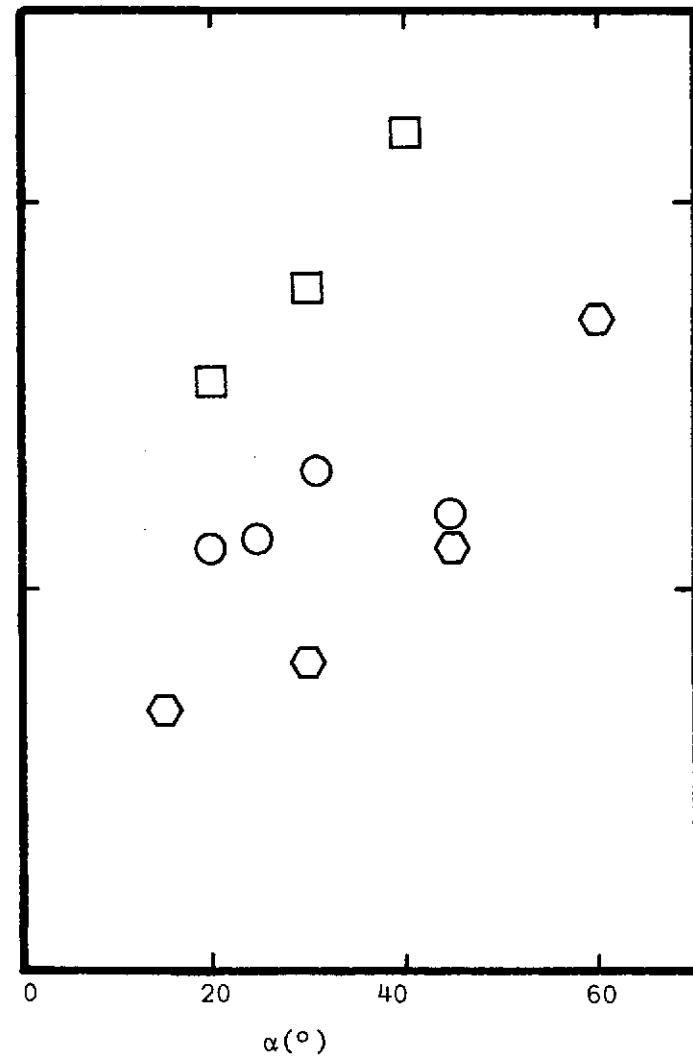
$$M_\infty = 6.86, Re_{\infty,D} = 3 \times 10^6$$

○ UTN2, $x = 0.39L$; □ UTN7, $x = 0.39L$

$$M_\infty = 4.57, Re_{\infty,L} = 8 \times 10^6$$



(a) Near the model nose

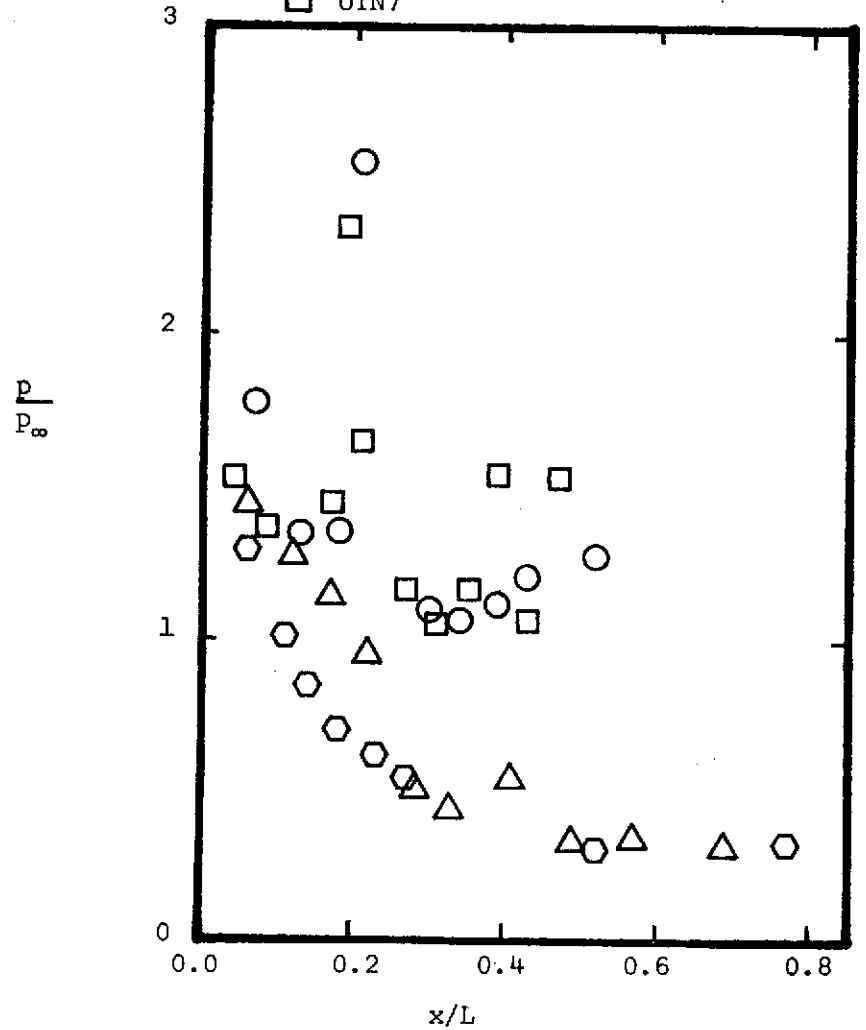


(b) Near the model base

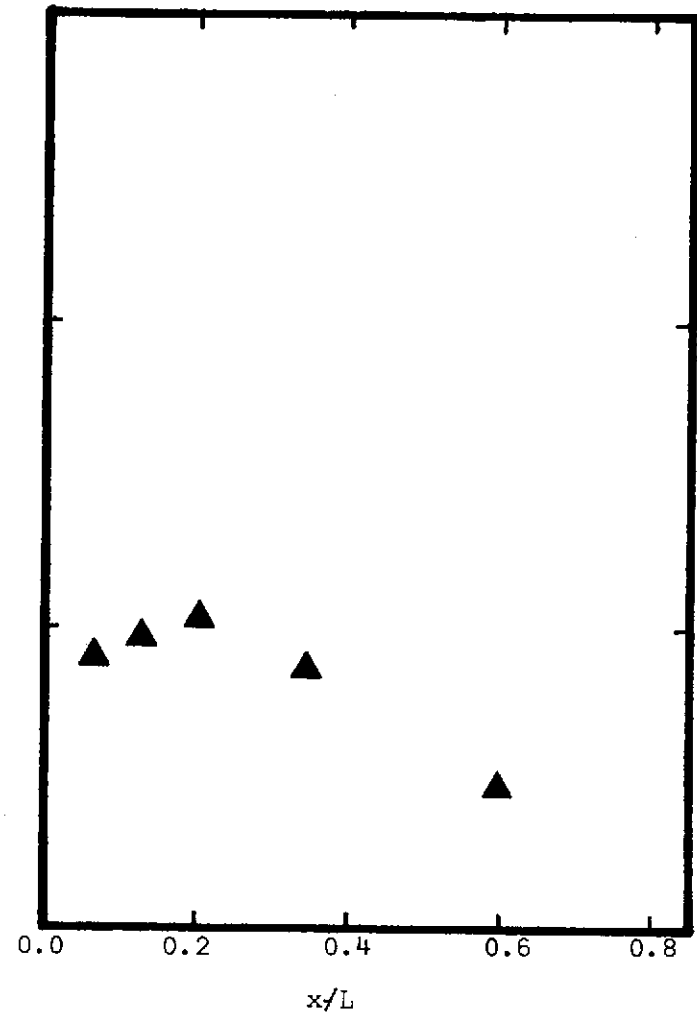
Figure 16. - Pressures from the leeward plane of symmetry as a function of alpha.

- ⬡ Langley configuration (Ref. 8)
- △ NYU configuration (Ref. 11)
- ▲ Slab delta-wing (Ref. 12)
- UTN2
- UTN7

α	M_∞	$Re_{\infty,L}$
20°	6	5.2×10^6
20°	6	5.2×10^6
20.4°	6.85	2.1×10^6 (max.)
19.5°	4.97	9.5×10^6
19.5°	4.97	8.0×10^6



(a) Shuttle configurations

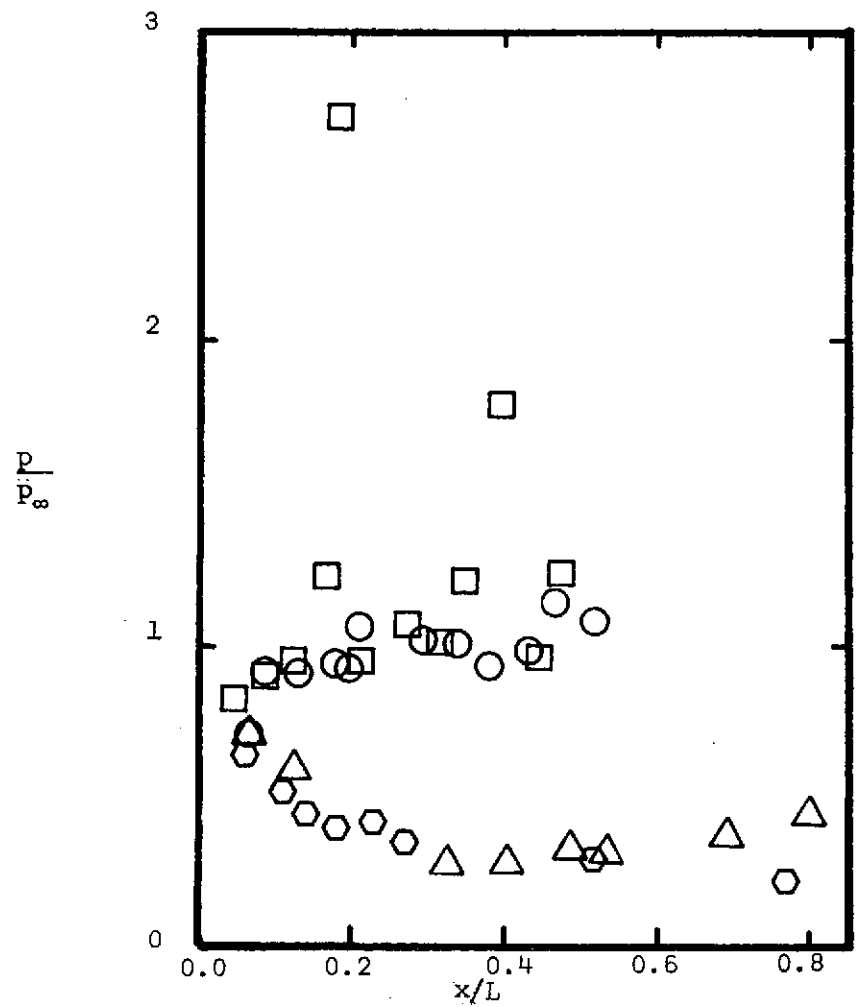


(b) Slab delta-wing

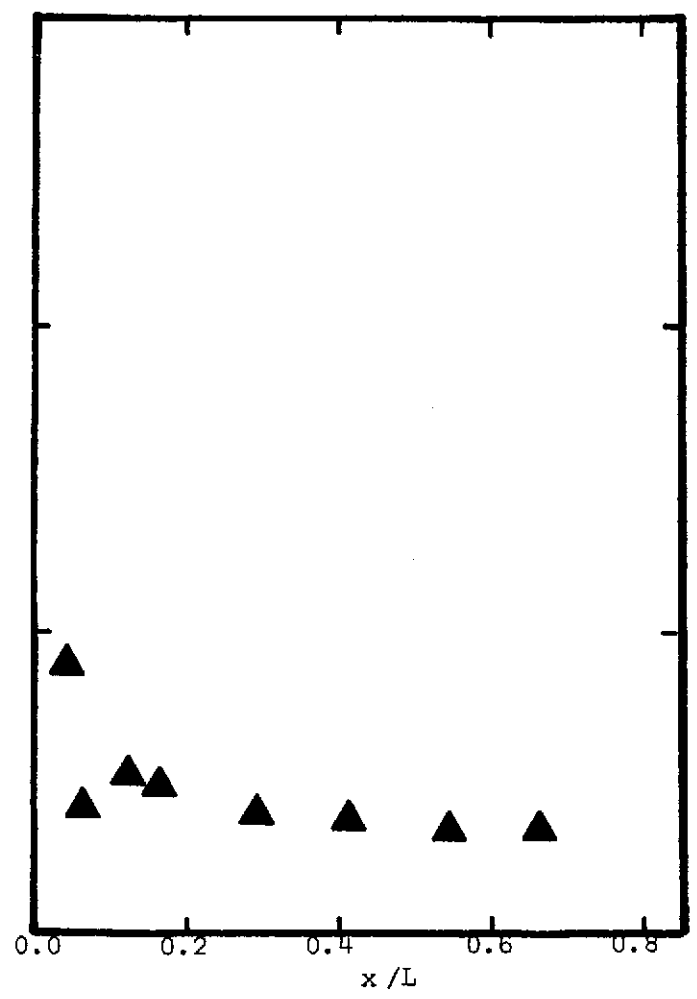
Figure 17. - Pressure distribution from the leeward pitch-plane for a variety of configurations at an alpha of 20° (nominal).

- Langley configuration (Ref. 8)
- △ NYU configuration (Ref. 11)
- ▲ Slab delta-wing (Ref. 12)
- UTN2
- UTN7

40°	6	6.9×10^6
40°	6	5.2×10^6
41.4	6.85	2.1×10^6 (max.)
43	4.97	9.5×10^6
40	4.97	9.5×10^6



(a) Shuttle configurations



(b) Slab delta-wing

Figure 18. - Pressure distribution from the leeward pitch-plane for a variety of configurations at alpha of 40° (nominal).